arXiv:2210.09883v1 [quant-ph] 18 Oct 2022

Exhaustive search for optimal molecular geometries using imaginary-time evolution on a quantum computer

Taichi Kosugi,[1,2,*] Hirofumi Nishi,[1,2] and Yu-ichiro Matsushita[1,2,3]

[1] *Laboratory for Materials and Structures, Institute of Innovative Research, Tokyo Institute of Technology, Yokohama 226-8503, Japan*
[2] *Quemix Inc., Taiyo Life Nihombashi Building, 2-11-2, Nihombashi Chuo-ku, Tokyo 103-0027, Japan*
[3] *Quantum Material and Applications Research Center, National Institutes for Quantum Science and Technology, 2-12-1, Ookayama, Meguro-ku, Tokyo 152-8552, Japan*

(Dated: October 19, 2022)

We propose a nonvariational scheme for geometry optimization of molecules for the first-quantized eigensolver, a recently proposed framework for quantum chemistry using the probabilistic imaginary-time evolution (PITE) on a quantum computer. While the electrons in a molecule are treated in the scheme as quantum mechanical particles, the nuclei are treated as classical point charges. We encode both electronic states and candidate molecular geometries as a superposition of many-qubit states, leading to quantum advantage. The histogram formed by outcomes of repeated measurements gives the global minimum of the energy surface. We demonstrate that the circuit depth scales as $\mathcal{O}(n_e^2 \mathrm{poly}(\log n_e))$ for the electron number n_e, which can be reduced to $\mathcal{O}(n_e \mathrm{poly}(\log n_e))$ if extra $\mathcal{O}(n_e \log n_e)$ qubits are available. We corroborate the scheme via numerical simulations. The new efficient scheme will be helpful for achieving scalability of practical quantum chemistry on quantum computers. As a special case of the scheme, a classical system composed only of charged particles is admitted. We also examine the scheme adapted to variational calculations that prioritize saving circuit depths for noisy intermediate-scale quantum (NISQ) devices.

I. INTRODUCTION

Modern computational designing of materials[1] and proteins[2] and drug discovery[3] often involve atomistic simulations for distinguishing microscopic subtleties rather than coarse-grained models. In order for such simulations to be as quantitatively reliable as possible, electronic-structure calculations based on the density functional theory[4, 5] or wave function theories[6] have to be performed to optimize the geometries of solids and molecules in their ground states. Although target systems diverse in the numbers of atoms and the elements are found in physics, chemistry, and biochemistry, there are mainly two kinds of approaches for finding the optimal geometry of a molecule on a classical computer: the energy-based approaches and the force-based ones.

The first approaches are simply based on the calculated total energies of all the candidate geometries. The procedure in a naive form typically begins with deciding upon the discretization of positions for each nucleus and calculates the total energies of all the possible geometries. Although this approach leads to exhaustive search for the optimal geometry among all the candidates and the search can be easily parallelized for many classical computers, the required computational resources grow exponentially with respect to the size of a target molecule. This notorious scaling makes the naive energy-based approach an impractical choice for systems of practical interest.

The second approaches are based on the forces acting on nuclei within the Born–Oppenheimer (BO) approximation. Such an optimization procedure for a target molecule is performed by calculating not only the total energy but also the forces acting on the constituent nuclei. More precisely, the procedure usually calculates the Hellmann–Feynman forces[7] and, if necessary, the Pulay forces[8] for compensating the incompleteness of adopted basis set. These forces can be calculated with only small additional computational resources for the total-energy calculation. The nuclear positions are updated iteratively according to the forces until convergence. The steepest-descent method and the conjugate-gradient method are the force-based approaches in the simplest forms. The updating process in these methods, however, is not parallelizable in principle. In addition, the search is prone to get stuck in a local minimum on the energy surface. Various elaborate force-based approaches have been proposed so far to achieve efficient and robust optimization of molecular geometries. For details, see, e.g., Ref. [9].

While quantum computation has been regarded as a promising alternative for storing many-electron wave functions living in a huge Hilbert space[10] since long before the advent of quantum computers, we find that geometry optimization of electronic systems is still going through the phase of establishing basic techniques, on the contrary to classical computation. Hirai et al. [11] proposed recently a method within the first-quantized formalism[12–14] by finding the lowest-energy geometry based on the imaginary-time evolution (ITE) with variational parameters[15–17] for nonadiabatically coupled electrons and nuclei. Their approach, which we refer to as the variational ITE (VITE) in what follows, is a kind of

* kosugi.taichi@gmail.com

the variational quantum eigensolver (VQE)[18, 19]. The major difference between our approach described later and their approach exists in how the qubits for nuclear degrees of freedom are used: we use them to encode the nuclear positions as classical data instead of their femtometer scale wave functions, so that we perform exhaustive search for the optimum among candidates via quantum parallelism.

Since the prevalent paradigm of electronic-structure calculations on classical computers has been developed primarily for computing the total energies of systems built up of electrons and nuclei, we might overlook the important fact, that is, there is no need for knowing the values of the total energies of candidate geometries to find the optimal one. We can find it only by knowing which geometry has the unknown lowest energy. Given this fact and the first-quantized eigensolver (FQE)[20], that is a recently proposed framework based on the probabilistic ITE (PITE) for nonvariational energy minimization in quantum chemistry, we develop in this paper a quantum algorithm for efficient geometry optimization that outperforms classical ones. Although the second-quantized formalism is useful for calculating the dynamical properties related to excitation processes of a molecule where the electron number can increase and decrease[21, 22], the first-quantized formalism for finding the ground state is known to offer better scaling of operation numbers[20]. As demonstrated later, this characteristics is inherited even when the geometry optimization is involved.

II. METHODS

A. First-quantized formalism and qubits

1. Setup

Let us consider a molecular system consisting of n_e electrons and $n_{\rm nucl}$ nuclei. We treat the electrons as quantum mechanical particles, while the nuclei as classical point charges with their positions fixed at $\boldsymbol{R}_\nu$ ($\nu = 0, \ldots, n_{\rm nucl}-1$). These two kinds of particles interact with each other via pairwise interactions v dependent only on the distance between two particles, as depicted in Fig. 1.

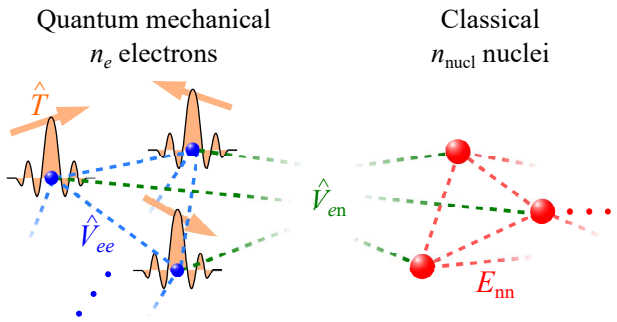

FIG. 1. Setup of a geometry optimization problem considered in this paper. We treat the n_e electrons contained in a target molecule as quantum mechanical particles having the kinetic energies $\hat{T}$, while the $n_{\rm nucl}$ nuclei as fixed classical point charges. The Hamiltonian of the total system involves the electron-electron interactions $\hat{V}_{ee}$, the electron-nucleus interactions $\hat{V}_{\rm en}$, and the nucleus-nucleus interactions $E_{\rm nn}$. The electrons can feel an external field $\hat{V}_{\rm ext}$.

The Hamiltonian of the total system is then given by

$$\mathcal{H}\left(\{\boldsymbol{R}_\nu\}_\nu\right) = \underbrace{\sum_{\ell=0}^{n_e-1} \frac{\hat{\boldsymbol{p}}_\ell^2}{2m_e}}_{\equiv\hat{T}} + \underbrace{\frac{1}{2}\sum_{\substack{\ell,\ell'=0\\(\ell\neq\ell')}}^{n_e-1} v\left(|\hat{\boldsymbol{r}}_\ell - \hat{\boldsymbol{r}}_{\ell'}|\right)}_{\equiv\hat{V}_{ee}}$$
$$+ \underbrace{\sum_{\ell=0}^{n_e-1}\sum_{\nu=0}^{n_{\rm nucl}-1} -Z_\nu v\left(|\hat{\boldsymbol{r}}_\ell - \boldsymbol{R}_\nu|\right)}_{\equiv\hat{V}_{\rm en}}$$
$$+ \underbrace{\frac{1}{2}\sum_{\substack{\nu,\nu'=0\\(\nu\neq\nu')}}^{n_{\rm nucl}-1} Z_\nu Z_{\nu'} v\left(|\boldsymbol{R}_\nu - \boldsymbol{R}_{\nu'}|\right)}_{\equiv E_{\rm nn}} + \underbrace{\sum_{\ell=0}^{n_e-1} v_{\rm ext}\left(\hat{\boldsymbol{r}}_\ell\right)}_{\equiv\hat{V}_{\rm ext}}, \quad (1)$$

where the nuclear positions appear as parameters. $\hat{T}$ is the kinetic-energy operator of electrons. $m_e = 1$ is the electron mass. All the quantities in this paper are in atomic units unless otherwise stated. $\hat{\boldsymbol{r}}_\ell$ and $\hat{\boldsymbol{p}}_\ell$ are the position and momentum operators, respectively, of the ℓth electron. Z_ν is the charge of the νth nucleus, while that of an electron is -1. We can introduce a position-dependent external field $v_{\rm ext}$ felt by each electron.

Although we adopted the common interaction v for $\hat{V}_{\rm ee}$, $\hat{V}_{\rm en}$, and $\hat{V}_{\rm nn}$ for simplicity, distinct interactions for them could be introduced with only small modifications to discussion below. Also, the formulations for one- and two-dimensional spaces will be possible similarly to the three-dimensional case.

2. Encoding of many-electron states

We encode the n_e-electron wave function in real space by using n_{qe} qubits for each direction per electron, as

usual in the first-quantized formalism[12–14, 20, 23, 24], or equivalently the grid-based formalism. We refer to the $3n_e n_{qe}$ qubits collectively as the electronic register.

We generate uniform grid points in a cubic simulation cell of size L to encode the normalized many-electron spatial wave function ψ by using the register as

$$|\psi\rangle = \Delta V^{n_e/2} \sum_{\boldsymbol{k}_0,\ldots,\boldsymbol{k}_{n_e-1}} \psi(\boldsymbol{r}^{(\boldsymbol{k}_0)},\ldots,\boldsymbol{r}^{(\boldsymbol{k}_{n_e-1})}) \cdot |\boldsymbol{k}_0\rangle_{3n_{qe}} \otimes \cdots \otimes |\boldsymbol{k}_{n_e-1}\rangle_{3n_{qe}}, \quad (2)$$

where $\boldsymbol{k}_\ell$ is the three integers specifying the position eigenvalue $(k_{\ell x}\boldsymbol{e}_x + k_{\ell y}\boldsymbol{e}_y + k_{\ell z}\boldsymbol{e}_z)\Delta x$ for the ℓth electron. $\Delta x \equiv L/N_{qe}$ is the spacing of $N_{qe} \equiv 2^{n_e}$ grid points for each direction. We introduced the volume element $\Delta V \equiv \Delta x^3$ for the normalization of $|\psi\rangle$.

3. *Encoding of possible molecular geometries*

Our method employs the superposition of $3n_{\rm nucl}n_{qn}$-qubit states, each of which encodes a combination $\{\Delta\boldsymbol{R}_\nu\}_\nu$ of displacements of nuclei from their original positions $\{\boldsymbol{R}_{\nu 0}\}_\nu$. We refer to the qubits for this superposition state collectively as the nuclear register.

We construct a composite system consisting of the nuclear and electronic registers and define an appropriate Hamiltonian, for which we perform energy minimization based on PITE to find the optimal combination $\{\Delta\boldsymbol{R}_\nu^{(\rm opt)}\}_\nu$ of displacements. To this end, we first decide upon the largest possible displacement $\Delta R_{\nu\mu\max}$ ($\mu = x, y, z$) in each direction μ for each nucleus ν. We introduce n_{qn} qubits for encoding the displacement in each direction for each nucleus. Specifically, we define the x position operator $\hat{\mathcal{R}}_{\nu x}$ of the νth nucleus such that each of the computational basis $|j_{\nu x}\rangle_{n_{qn}}$ ($j_{\nu x} = 0,\ldots,2^{n_{qn}}-1$) is the eigenstate as follows:

$$\hat{\mathcal{R}}_{\nu x}|j_{\nu x}\rangle_{n_{qn}} \equiv \left(R_{\nu 0x} + j_{\nu x}\frac{\Delta R_{\nu x\max}}{N_{qn}}\right)|j_{\nu x}\rangle_{n_{qn}}, \quad (3)$$

where $N_{qn} \equiv 2^{n_{qn}}$. The operators $\hat{\mathcal{R}}_{\nu y}$ and $\hat{\mathcal{R}}_{\nu z}$ for the y and z positions, respectively, are defined similarly. Our method thus uses the $3n_{\rm nucl}n_{qn}$ qubits for the nuclear positions and there exists one-to-one correspondence between the $N_{qn}^{3n_{\rm nucl}}$ computational basis vectors and the possible molecular geometries. It is noted that n_{qn} is a parameter that determines the resolution of the search for the optimal geometry and has no direct relation to the physical properties of the nuclei. Also, we emphasize here that we have introduced the nuclear register and the operators $\{\hat{\boldsymbol{\mathcal{R}}}_\nu\}_\nu$ not for encoding quantum states of nuclei, but for encoding the data for the nuclei as distinguishable classical particles.

Having defined the nuclear position operators, we rewrite the Hamiltonian in Eq. (1) simply by replacing the nuclear positions as c-numbers with the corresponding operators:

$$\mathcal{H}(\{\boldsymbol{R}_\nu\}_\nu) \to \mathcal{H}(\{\hat{\boldsymbol{\mathcal{R}}}_\nu\}_\nu), \quad (4)$$

leading to the new Hamiltonian for the $(3n_e n_{qe} + 3n_{\rm nucl}n_{qn})$-qubit system. E_{nn} has become the operator $\hat{V}_{\rm nn}$.

B. Circuits and measurements for optimal geometries

1. *Preparation of input state*

To generate a suitable initial state for a specific target molecule, we introduce two unitaries $U_{\rm guess}$ and $U_{\rm ref}$ prior to the energy minimization procedure.

$U_{\rm guess}$ is defined such that it acts on the initialized nuclear register to generate the superposition of $N_{qn}^{3n_{\rm nucl}}$ possible geometries having desired weights, as shown in Fig. 2(a):

$$U_{\rm guess}|0\rangle_{3n_{\rm nucl}n_{qn}} = \sum_{\boldsymbol{j}_0,\ldots,\boldsymbol{j}_{n_{\rm nucl}-1}} \sqrt{w_{0\boldsymbol{J}}}|\boldsymbol{j}_0\rangle_{3n_{qn}} \otimes \cdots \otimes |\boldsymbol{j}_{n_{\rm nucl}-1}\rangle_{3n_{qn}}, \quad (5)$$

where each term in the summation on the RHS represents the displacements of nuclei. $\boldsymbol{J}$ represents collectively the $3n_{\rm nucl}n_{qn}$ integers $\boldsymbol{j}_0,\ldots,\boldsymbol{j}_{n_{\rm nucl}-1}$ for Eq. (3). We should adopt the weight $w_{0\boldsymbol{J}}$ of each geometry specified by $\boldsymbol{J}$ based on an initial guess that gives rise to large weights for plausible molecular geometries. If we have no information about which geometries are plausible, the uniform superposition of all the possible geometries generated by the Hadamard gate on each qubit will be suitable: $U_{\rm guess} = H^{\otimes 3n_{\rm nucl}n_{qn}}$ for $w_{0\boldsymbol{J}} = 1/N_{qn}^{3n_{\rm nucl}}$.

$U_{\rm ref}$ is defined such that it acts on the nuclear register and the initialized electronic register to generate the desired reference electronic state $|\psi_{\rm ref}[\boldsymbol{J}]\rangle$ for the indistinguishable particles[25, 26] in the geometry specified by $\boldsymbol{J}$, as shown in Fig. 2(b):

$$U_{\rm ref}\Big(\overbrace{|0\rangle_{3n_e n_{qe}}}^{\text{Electrons}} \otimes \overbrace{|\boldsymbol{J}\rangle_{3n_{\rm nucl}n_{qn}}}^{\text{Nuclei}}\Big) = |\psi_{\rm ref}[\boldsymbol{J}]\rangle \otimes |\boldsymbol{J}\rangle_{3n_{\rm nucl}n_{qn}}. \quad (6)$$

We need to adopt good $U_{\rm guess}$ and $U_{\rm ref}$ so that the prepared initial state for the subsequent energy minimization achieves rapid convergence.

2. *Energy minimization for finding optimal geometry*

We construct the circuit $\mathcal{C}_{\rm opt}$ for the entire optimization procedure within FQE, as shown in Fig. 2(c). This circuit first generates the input state

$$|\Psi_0\rangle = \sum_{\boldsymbol{J}} \sqrt{w_{0\boldsymbol{J}}}|\psi_{\rm ref}[\boldsymbol{J}]\rangle \otimes |\boldsymbol{J}\rangle_{3n_{\rm nucl}n_{qn}} \quad (7)$$

for the subsequent PITE steps implemented by the $\mathcal{C}_{\rm PITE}$ circuits. The number $n_{\rm steps}$ of steps needs to be large

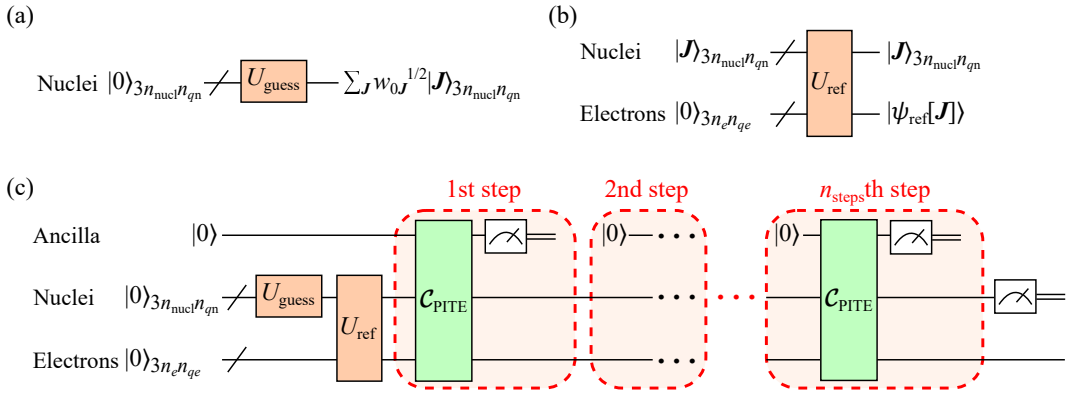

FIG. 2. (a) Initial-guess gate $U_{\rm guess}$ for assigning the weight $w_{0\boldsymbol{J}}$ to each molecular geometry specified by $\boldsymbol{J}$. (b) Reference state gate $U_{\rm ref}$ for generating the reference electronic state $|\psi_{\rm ref}[\boldsymbol{J}]\rangle$ for the geometry specified by $\boldsymbol{J}$. (c) Circuit $\mathcal{C}_{\rm opt}$ for the entire optimization procedure within FQE. It contains $n_{\rm steps}$ PITE steps for energy minimization governed by the Hamiltonian $\mathcal{H}$ of the system made up of the electrons and the nuclei. The ancilla qubit is for observing the success or failure state at each PITE step.

enough so that all the excited states of the composite system have satisfactorily diminished. It has also to be, however, small compared with the coherence time of quantum hardware being used.

Since we are working with the first-quantized formalism, the coefficients of computational bases of the electronic and nuclear registers give the state of the composite system as

$$|\Psi\rangle = \sum_{\boldsymbol{k}_0,\ldots,\boldsymbol{k}_{n_e-1}} \sum_{\boldsymbol{J}} c_{\boldsymbol{K},\boldsymbol{J}} \overbrace{|\boldsymbol{K}\rangle_{3n_e n_{qe}}}^{\text{Electrons}} \otimes \overbrace{|\boldsymbol{J}\rangle_{3n_{\rm nucl}n_{qn}}}^{\text{Nuclei}}, \quad (8)$$

where $\boldsymbol{K}$ represents collectively the $3n_e n_{qe}$ integers $\boldsymbol{k}_0,\ldots,\boldsymbol{k}_{n_e-1}$. The normalization condition forces the coefficients to satisfy $\sum_{\boldsymbol{K},\boldsymbol{J}}|c_{\boldsymbol{K},\boldsymbol{J}}|^2 = 1$. The weight of geometry $\boldsymbol{J}$ contained in $|\Psi\rangle$ is given by $w_{\boldsymbol{J}} = \sum_{\boldsymbol{K}}|c_{\boldsymbol{K},\boldsymbol{J}}|^2$. By defining the renormalized coefficients $c_{\boldsymbol{K}}[\boldsymbol{J}] \equiv c_{\boldsymbol{K},\boldsymbol{J}}/\sqrt{w_{\boldsymbol{J}}}$, we write the normalized electronic state for a fixed geometry $\boldsymbol{J}$ as

$$|\psi[\boldsymbol{J}]\rangle = \sum_{\boldsymbol{K}} c_{\boldsymbol{K}}[\boldsymbol{J}]|\boldsymbol{K}\rangle_{3n_e n_{qe}}. \quad (9)$$

We can then rewrite the state of composite system in Eq. (8) as

$$|\Psi\rangle = \sum_{\boldsymbol{J}} \sqrt{w_{\boldsymbol{J}}}|\psi[\boldsymbol{J}]\rangle \otimes |\boldsymbol{J}\rangle_{3n_{\rm nucl}n_{qn}}. \quad (10)$$

By comparing this expression and Eq. (7), we understand that $w_{\boldsymbol{J}}$ and $|\psi[\boldsymbol{J}]\rangle$ in the case of the input state are equal to $w_{0\boldsymbol{J}}$ and $|\psi_{\rm ref}[\boldsymbol{J}]\rangle$, respectively, for each $\boldsymbol{J}$.

When we perform a measurement on the nuclear register comprising $|\Psi_s\rangle$ of the form in Eq. (10) immediately after the sth step, the probability for observing the molecular geometry corresponding to a specific $\boldsymbol{J}$ is clearly $w_{s\boldsymbol{J}}$, which is the weight of geometry $\boldsymbol{J}$ contained in $|\Psi_s\rangle$. The composite state having undergone sufficiently many PITE steps will thus provide the lowest-energy geometry with the highest probability:

$$\boldsymbol{J}^{(\rm opt)} = \arg\max_{\boldsymbol{J}} w_{n_{\rm steps}\boldsymbol{J}}, \quad (11)$$

from which the optimal displacements $\{\Delta\boldsymbol{R}_\nu^{(\rm opt)}\}_\nu$ are calculated from Eq. (3). In practice, $\boldsymbol{J}^{(\rm opt)}$ can be found by drawing a histogram of observed values of $\boldsymbol{J}$ from repeated measurements.

While the required number of qubits for encoding the many-electron wave function scales linearly with respect to n_e for a fixed resolution, the required memory for the simulation of the wave function on a classical computer scales exponentially. Furthermore, our approach treats all the possible molecular geometries, whose number grows exponentially in $n_{\rm nucl}$ and n_{qn}, simultaneously. These facts highlight the quantum advantage of our approach.

In the actual optimization procedure for a given molecule, we will be confronted with a dilemma: while a more accurate prediction of the optimal geometry requires finer discretization of nuclear displacements, such discretization inevitably leads to smaller energy differences between "neighboring" candidate geometries, which are more difficult to detect via the finite number of PITE steps. The histogram of observed geometries will thus exhibit a shape formed by multiple maxima, each of which has a finite width around it and corresponds to possibly one of the local minima on the energy surface of the molecule. If we want to predict one of the local-minimum geometry more accurately, we should start newly an optimization procedure by restricting the nuclear displacements within the vicinity of the local minimum, only for which the nuclear register is spent.

3. Comparison with nonadiabatic treatment

Kassal et al.[14] demonstrated that nonadiabatic treatment of nuclei as quantum mechanical particles in a molecule as well as the electrons, is computationally much more efficient for a chemical-reaction simulation than the BO approximation, except for the smallest molecules. On the other hand, one finds that the classical treatment of nuclei in our approach for geometry optimization is more efficient than the nonadiabatic treatment for the following reasons. If we used the $3n_{\mathrm{nucl}}n_{qn}$ qubits for the nuclei as quantum mechanical particles to encode their wave function, the grid spacing in the simulation cell has to be on the order of femtometer (fm) to detect the finite width of wave function of each nucleus. The grid spacing Δx for electronic wave function has also to be on the same order for a reliable simulation, while that may be on the order of Å in our original approach. The required number n_{qn} of qubits for the nonadiabatic treatment is thus larger than that for the classical treatment roughly by $\log_2(\text{Å/fm}) \approx 16.6$, which is also the case for n_{qe}. Furthermore, we will then give up the superposition of candidate geometries since the nuclear register has already been reserved for the many-nucleus wave function. Therefore we have to perform the energy minimization starting from some single initial geometry. These considerations indicate that the classical treatment of nuclei is practically more favorable than the nonadiabatic one unless the result of optimization is affected qualitatively by the nonadiabatic treatment.

4. Optimization for classical point charges

As a special case of our scheme described above, we can perform geometry optimization for a classical system composed of point charges. To be specific, the Hamiltonian for such a system is defined by incorporating only the terms between the nuclei from the original Hamiltonian: $\mathcal{H}_{\mathrm{cl}}(\{\hat{\boldsymbol{\mathcal{R}}}_\nu\}_\nu) \equiv \hat{V}_{\mathrm{nn}}$. The circuit for the entire procedure in this case is depicted in Fig. 3, as a special case of Fig. 2(c).

We can also perform the scheme by adopting empirical anisotropic potentials of the form $v(\boldsymbol{R}_\nu - \boldsymbol{R}_{\nu'})$ depending explicitly on the relative vector between effective nuclei. Although such artificial potentials may lead to more complicated circuits for $e^{-i\hat{V}_{nn}\Delta t}$ than the bare-Coulomb potentials, the scaling of circuit depths with respect to n_{nucl} and n_{qn} discussed below will not be affected. It is because how complicated the functional forms of v are has nothing to do with n_{nucl} and n_{qn}.

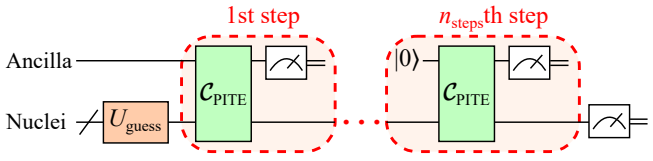

FIG. 3. Circuit for the geometry optimization procedure for classical point charges. The PITE circuit $\mathcal{C}_{\mathrm{PITE}}$ in this case is for $\mathcal{H}_{\mathrm{cl}}(\{\hat{\boldsymbol{\mathcal{R}}}_\nu\}_\nu)$.

C. Implementation of PITE circuit

1. Scaling of depths with respect to numbers of particles

The PITE circuit $\mathcal{C}_{\mathrm{PITE}}$ consists mainly of the controlled RTE operators.[20] We implement the RTE operator $e^{-i\mathcal{H}\Delta t}$ for a time step Δt by employing the first-order Suzuki–Trotter as usual to decompose it approximately into the kinetic part $e^{-i\hat{T}\Delta t}$ and the position-dependent part $\exp[-i(\hat{V}_{ee}+\hat{V}_{\mathrm{en}}+\hat{V}_{\mathrm{nn}}+\hat{V}_{\mathrm{ext}})\Delta t]$. While the former can be implemented using the QFT-based techniques[20, 27, 28] as in the electrons-only cases, the latter is further decomposed exactly into the four parts, as shown in Fig. 4. The details of their implementation and the scaling of circuit depths with respect to the numbers of electrons and nuclei are explained in Appendix A 1. It is clear from the figure that the partial circuits for $e^{-i\hat{V}_{ee}\Delta t}$ and $e^{-i\hat{V}_{\mathrm{nn}}\Delta t}$ are deeper than those for $e^{-i\hat{V}_{\mathrm{en}}\Delta t}$ and $e^{-i\hat{V}_{\mathrm{ext}}\Delta t}$ from the viewpoint of scaling with respect to n_e and n_{nucl}.

2. Scaling of depths with respect to resolution of discretization

Although our PITE circuit does not assume specific implementation of the phase gates comprising $e^{-i\hat{V}_{ee}\Delta t}$, $e^{-i\hat{V}_{\mathrm{en}}\Delta t}$, and $e^{-i\hat{V}_{\mathrm{nn}}\Delta t}$, we propose here a plausible alternative by exploiting the fact that the pairwise interaction v is common to these three types of evolution and depends only on the distance between particles. By dividing the task we have to do into the computation of distances between the particles and that of the phases for evolution, we find the systematic construction of the circuits, as explained in Appendix A 2. Fig. 5 shows the circuit that implements the pairwise e-e phase gate $U_{ee}(\Delta t)$, defined in Eq. (A1) as a building block of $e^{-i\hat{V}_{ee}\Delta t}$ operation. The pairwise phase gates $U_{\mathrm{en}}^{(\nu)}(\Delta t)$ and $U_{\mathrm{nn}}^{(\nu,\nu')}(\Delta t)$ as building blocks of $e^{-i\hat{V}_{\mathrm{en}}\Delta t}$ and $e^{-i\hat{V}_{\mathrm{nn}}\Delta t}$, respectively, can also be implemented similarly. For example, the circuit for computing the distance can be implemented efficiently by combining the addition[29–31], multiplication[32–34], and square root[35].

If we approximate the functional shape of the interac-

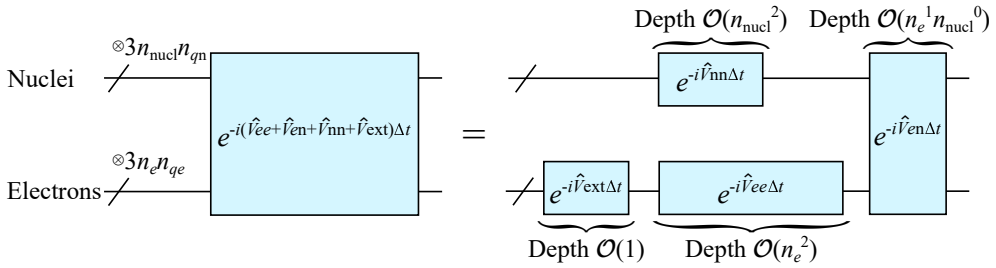

FIG. 4. RTE operator $e^{-i\mathcal{H}\Delta t}$ for a time step Δt required in the $\mathcal{C}_{\rm PITE}$ circuit is decomposed into the kinetic part and the position-dependent part via the first-order Suzuki–Trotter. The latter is shown in the left part of this figure, which is further decomposed into the evolution operators generated by $\hat{V}_{ee}, \hat{V}_{en}, \hat{V}_{nn}$, and $\hat{V}_{ext}$ separately, as shown in the right part. The scaling of depths with respect to the numbers of electrons and nuclei are also shown.

tion v as a simple or a piecewisely defined polynomial, the interaction phase gates $U_{{\rm int},\kappa}(\Delta t)$ ($\kappa = ee, en, nn$), defined in Eq. (A12), can be implemented with polynomial depths[28, 36] in the numbers $n_\kappa^{(\rm d)}$ of qubits for the distance registers. Although $n_\kappa^{(\rm d)}$ can be set independently of n_{qe} and n_{qn}, it is suitable to set them such that the resolutions induced by the former are on the same order as by the latter: $n_{ee}^{(\rm d)} = \mathcal{O}(n_{qe}), n_{en}^{(\rm d)} = \mathcal{O}(\max(n_{qe}, n_{qn}))$, and $n_{nn}^{(\rm d)} = \mathcal{O}(n_{qn})$. These considerations tell us that the pairwise phase gates $U_{ee}(\Delta t), U_{en}^{(\nu)}(\Delta t)$, and $U_{nn}^{(\nu,\nu')}(\Delta t)$ can be implemented with polynomial depths in n_{qe} and n_{qn}.

As discussed in Ref. [20], the number of qubits for the electronic wave function with a resolution Δx typically scales as $n_{qe} = \mathcal{O}(\log(n_e^{1/3}/\Delta x))$. On the other hand, that for the nuclear displacements scales as $n_{qn} = \mathcal{O}(\log(\Delta R_{\rm max}/\Delta R))$ for typical values of a resolution ΔR and the maximal displacement $\Delta R_{\rm max}$. The circuit depth for the evolution generated by $\hat{V}_{ee}$ is thus found to scale as

$$\mathrm{depth}(e^{-i\hat{V}_{ee}\Delta t}) = \mathcal{O}\left(n_e^2 \mathrm{poly}\left(\log\frac{n_e^{1/3}}{\Delta x}\right)\right). \quad (12)$$

[See Fig. 4] That for $\hat{V}_{nn}$ scales as

$$\mathrm{depth}(e^{-i\hat{V}_{nn}\Delta t}) = \mathcal{O}\left(n_{\rm nucl}^2 \mathrm{poly}\left(\log\frac{\Delta R_{\rm max}}{\Delta R}\right)\right). \quad (13)$$

That for $\hat{V}_{en}$ scales as

$$\mathrm{depth}(e^{-i\hat{V}_{en}\Delta t}) = \mathcal{O}\left(n_e \mathrm{poly}\left(\max\left(\log\frac{n_e^{1/3}}{\Delta x}, \log\frac{\Delta R_{\rm max}}{\Delta R}\right)\right)\right). \quad (14)$$

Also, that for $\hat{V}_{\rm ext}$ scales as

$$\mathrm{depth}(e^{-i\hat{V}_{\rm ext}\Delta t}) = \mathcal{O}\left(\mathrm{poly}\left(\log\frac{n_e^{1/3}}{\Delta x}\right)\right). \quad (15)$$

Recalling the fact that n_e is much larger than $n_{\rm nucl}$ despite their common scaling for a generic molecule, we find that $e^{-i\hat{V}_{ee}\Delta t}$ dominates the scaling of circuit depth of the entire position-dependent evolution when $\Delta R_{\rm max}$ and ΔR are fixed. In fact, the $e^{-i\hat{V}_{nn}\Delta t}$ circuit does not contribute to the total depth since it and $e^{-i\hat{V}_{ee}\Delta t}$, which is much deeper than it, can be performed in parallel, as seen in Fig. 4. Since the circuit depth of the QFT-based kinetic evolution scales as[20]

$$\begin{aligned}\mathrm{depth}(e^{-i\hat{T}\Delta t}) &= \mathcal{O}\left(n_e^0 n_{qe}^2\right) \\ &= \mathcal{O}\left(\left(\log\frac{n_e^{1/3}}{\Delta x}\right)^2\right), \end{aligned} \quad (16)$$

the scaling coming from the electron-electron interactions, given by Eq. (12), is dominant even in the entire RTE circuit:

$$\mathrm{depth}(e^{-i\mathcal{H}\Delta t}) = \mathcal{O}\left(n_e^2 \mathrm{poly}\left(\log\frac{n_e^{1/3}}{\Delta x}\right)\right). \quad (17)$$

Since the PITE circuit contains the controlled RTE operations, its depth exhibits the same scaling: $\mathrm{depth}(\mathcal{C}_{\rm PITE}) = \mathcal{O}(\mathrm{depth}(e^{-i\mathcal{H}\Delta t}))$.

If the same number $3n_e n_{qe}$ of extra qubits as in the electronic register are available, the scaling of depth for $e^{-i\hat{V}_{ee}\Delta t}$ can be reduced. Specifically, n_e^2 on the RHS in Eq. (12) becomes n_e via the technique described in Appendix A 3. (See also Ref. [23]) The scaling of depth for $e^{-i\hat{V}_{nn}\Delta t}$ can be reduced similarly if the same number of qubits as in the nuclear register are available. With these techniques, the depth of the entire RTE circuit is

$$\mathrm{depth}(e^{-i\mathcal{H}\Delta t}) = \mathcal{O}\left(n_e \mathrm{poly}\left(\log\frac{n_e^{1/3}}{\Delta x}\right)\right), \quad (18)$$

instead of Eq. (17).

It is noted that, if the number of available extra qubits is $\mathcal{O}(n_e^2 n_{qe})$, the technique proposed in Ref. [23] leads to more drastic reduction of the depth: n_e^2 on the RHS in Eq. (12) becomes 1.

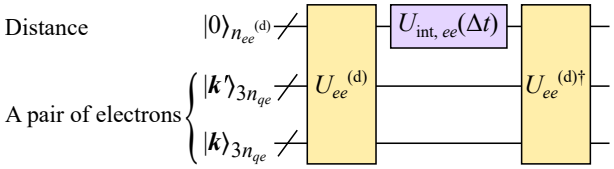

FIG. 5. Circuit that implements the pairwise e-e phase gate $U_{ee}(\Delta t)$ as a building block of $e^{-i\hat{V}_{ee}\Delta t}$ operation. $U_{ee}^{(\mathrm{d})}$ defined in Eq. (A9) computes the distance between two electrons at $\boldsymbol{r}^{(\boldsymbol{k})}$ and $\boldsymbol{r}^{(\boldsymbol{k}')}$, which is then stored into the distance register consisting of $n_{ee}^{(\mathrm{d})}$ qubits. The interaction phase gate $U_{\mathrm{int},ee}(\Delta t)$ defined in Eq. (A12) refers to the distance register to generate the phase required for the evolution coming from the electron pair. The inverse of $U_{ee}^{(\mathrm{d})}$ performs uncomputation for disentangling the distance register from the electronic register.

III. APPLICATIONS

A. PITE for a model LiH molecule

1. Setup

We consider here an effective model of a lithium hydride molecule in one-dimensional space used in Ref. [37]. This model regards the $1s$ electrons of the Li atom to be frozen so that the system consists of the two valence electrons, the H ion with $Z_{\mathrm{H}} = 1$, and the Li ion with $Z_{\mathrm{Li}} = 1$. The interactions between the particles are modelled basically by the soft-Coulomb interaction

$$v_{\mathrm{soft}}(r;\lambda) \equiv \frac{1}{\sqrt{\lambda^2 + r^2}}, \tag{19}$$

where r is the distance between two particles and the parameter λ measures the softness of the interaction. This family of potentials is often used for avoiding the singular behavior of the bare-Coulomb potential[38]. The adopted values for the interactions are as follows: $v_{ee}(r) = v_{\mathrm{soft}}(r;\lambda_{ee})$ between the electrons with $\lambda_{ee}^2 = 0.6$, $v_{e\mathrm{H}}(r) = v_{\mathrm{soft}}(r;\lambda_{e\mathrm{H}})$ between each electron and the H ion with $\lambda_{e\mathrm{H}}^2 = 0.7$, $v_{e\mathrm{Li}}(r) = v_{\mathrm{soft}}(r;\lambda_{e\mathrm{Li}})$ between each electron and the Li ion with $\lambda_{e\mathrm{Li}}^2 = 2.25$, and $v_{\mathrm{LiH}}(r) = v_{\mathrm{soft}}(r;\lambda_{\mathrm{LiH}})$ between the ions with $\lambda_{\mathrm{LiH}}^2 \equiv \lambda_{e\mathrm{H}}^2 + \lambda_{e\mathrm{Li}}^2 - \lambda_{ee}^2 = 2.35$. The potential felt by each electron is thus $v_{en}(x) = -Z_{\mathrm{H}} v_{e\mathrm{H}}(|x - X_{\mathrm{H}}|) - Z_{\mathrm{Li}} v_{e\mathrm{Li}}(|x - X_{\mathrm{Li}}|)$, where X_{H} and X_{Li} are the positions of the H and Li ions, respectively.

2. Energy eigenstates

Figure 6(a) shows the energy eigenvalues of the molecule as functions of the bond length $d \equiv |X_{\mathrm{Li}} - X_{\mathrm{H}}|$ obtained by numerical diagonalization of the Hamiltonian matrix. By using $n_{qe} = 6$ qubits per electron for a simulation cell with $L = 15$, we obtained the equilibrium bond length $d_{\mathrm{eq}} = 1.55$, in reasonable agreement with that in the earlier paper[37]. Figure 6(b) shows the electron densities of the energy eigenstates obtained by numerical diagonalization for $d = d_{\mathrm{eq}}, 4$. For $d = d_{\mathrm{eq}}$, the electrons are localized near the H ion to exhibit the single-peak shape. For $d = 4$, on the other hand, they are localized at each ion, indicative of dissociation. We found for both bond lengths that the ground state $|\phi_{\mathrm{gs}}\rangle$ and the second excited state $|\phi_{\mathrm{ex2}}\rangle$ are symmetric under exchange of the spatial coordinates x_0 and x_1 of the two electrons, while the first excited state $|\phi_{\mathrm{ex1}}\rangle$ is antisymmetric under the exchange. Recalling that our encoding of wave functions does not incorporate explicitly the spin parts [see Eq. (2)], the ground state and the second excited state are spin-singlet states, while the first excited state is a spin-triplet state.

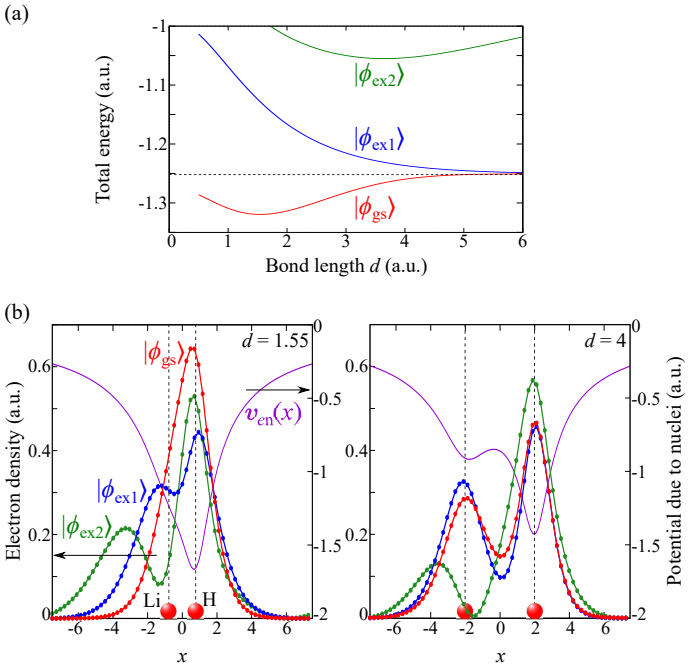

FIG. 6. (a) Energy eigenvalues of the LiH model system as functions of the bond length d obtained by numerical diagonalization. $|\phi_{\mathrm{gs}}\rangle$, $|\phi_{\mathrm{ex1}}\rangle$, and $|\phi_{\mathrm{ex2}}\rangle$ are the ground state, the first excited state, and the second excited state, respectively. The horizontal dashed line indicates the dissociation limit, that is, the sum of total energies for the isolated H and Li atoms. (b) Left panel shows the electron densities of the energy eigenstates for the equilibrium bond length d_{eq}. The vertical lines indicate the positions of the ions. The potential v_{en} felt by each electron due to the nuclei is also shown. The right panel is a similar plot for $d = 4$. The x coordinates in the figures have been shifted so that the midpoint of the bond is at the origin.

3. Geometry optimization

We performed simulations of geometry optimization among eight candidates represented by $n_{qn} = 3$ qubits. To be specific, we tried the bond lengths $d_J = 0.55 + 0.5J$ ($J = 0, \ldots, 7$). The amount of imaginary-time step does not need to be constant. For example, we can define it for the kth PITE step as

$$\Delta\tau_k = (1 - e^{-k/\kappa})(\Delta\tau_{\max} - \Delta\tau_{\min}) + \Delta\tau_{\min}, \quad (20)$$

so that it changes gradually from $\Delta\tau_{\min}$ to $\Delta\tau_{\max}$. κ determines the rate of change. We adopted $\Delta\tau_{\min} = 0.2, \Delta\tau_{\max} = 0.3$, and $\kappa = 8$ for the following simulations.

To find the optimal bond length for the ground state, we assigned a uniform weight distribution to the candidate geometries, for which we generated the initial spatial wave functions

$$\Psi_{\rm s}(x_0, x_1) \propto \exp\left(-\frac{(x_0 - X_{\rm m})^2 + (x_1 - X_{\rm m})^2}{w^2}\right) \quad (21)$$

for the geometries. $X_{\rm m} \equiv (X_{\rm H} + X_{\rm Li})/2$ is the midpoint of the bond and $w = 3$ is the width of the wave function. Since $\Psi_{\rm s}$ is symmetric under exchange of the electrons, it is for obtaining a spin singlet state. Figure 7(a) shows the weight w_J of each geometry J during the steps contained in the state $|\Psi\rangle$ for the composite system of the electrons and nuclei. The weight $w_{J,\rm gs}$ of the ground state $|\psi_{\rm gs}\rangle$ for each geometry is also shown in the figure. It is seen that the uniform distribution of weights in the initial state undergoes the deformation via the PITE steps. It has the peak around the geometry for $J = 2$ already after the 9th step, corresponding to the equilibrium bond length $d_{\rm eq}$. This peak structure becomes more prominent after the 19th step. These observations corroborate the validity of our generic scheme.

Using the fact that the ground state and the first excited state $|\psi_{\rm ex1}\rangle$ of this system have the different symmetry, we can perform geometry optimization for the first excited state. To this end, we adopted the initial spatial wave functions

$$\Psi_{\rm a}(x_0, x_1) \propto \frac{x_0 - x_1}{w}\Psi_{\rm s}(x_0, x_1) \quad (22)$$

for the geometries. Since $\Psi_{\rm a}$ is antisymmetric under exchange of the electrons, it is for obtaining a spin triplet state. The results are shown in Fig. 7(b). In contrast to the case of the ground state, the resultant weight distribution does not have a peak between $J = 0$ and 7, which lets the observer recognize that there exists no equilibrium bond length among the candidate geometries.

B. VITE for a model H_2^+ molecule

1. Setup

Since the essence of our approach is the superposition of nuclear-register states where the candidate geometries are encoded, geometry optimization based on VITE instead of PITE is straightforwardly formulated. To demonstrate that, we consider here an effective model of a hydrogen molecular ion in a one-dimensional space used in Ref. [39]. The charge of each ion is $Z_{\rm H} = 1$. Here, we also use the soft-Coulomb interaction defined in Eq. (19) to model the interactions between the particles. We adopt the softness $\lambda_{e\rm H}^2 = 1$ for the interaction $v_{e\rm H}(r)$ between the electron and each ion and $\lambda_{\rm HH}^2 = 1$ for $v_{\rm HH}(r)$ between the ions. The potential felt by the electron is thus $v_{en}(x) = -Z_{\rm H}v_{e\rm H}(|x - X_{\rm H\alpha}|) - Z_{\rm H}v_{e\rm H}(|x - X_{\rm H\beta}|)$, where $X_{\rm H\alpha}$ and $X_{\rm H\beta}$ are the positions of the H ions.

2. Ansatz

The VITE approach is explained briefly in Appendix B. Figure 8 shows our ansatz circuit for geometry optimization of the H_2^+ model system. We adopted the hardware-efficient connectivity[40] for the circuit, which is desirable for noisy intermediate-scale quantum (NISQ) devices due to shallow circuit depths. In addition, the accuracy of the quantum computation systematically improves by incrementing the repetition d of the layer. Here, we use the full coupling model; CZ gates connect every pair of qubits for entangling all qubits. We allocated $n_{q\rm nucl} = 3$ qubits for encoding the nuclear positions and $n_{qe} = 6$ qubits for encoding the single-electron wave function in a simulation cell with $L = 15$.

3. Geometry optimization

The VITE calculation was performed for candidates whose bond length were specified by $d_J = 0.5 + (7.5/8)J$ ($J = 0, \ldots, 7$). We simulated the updating process of variational parameters with $d = 12$ for 6000 VITE steps with $\Delta\tau = 0.01$. All the initial values of the variational parameters were set to random values. The expected energy of the trial state $|\Psi\rangle$ at each VITE step measured from the numerically exact ground state energy is shown in Fig. 9(a). We recognize the monotonic but slow decrease in the energy difference. Figure 9(b) shows the weights w_J of candidate geometries contained in the trial wave function at each VITE step. The weight of the most stable geometry labeled by $J = 2$ monotonically increases and reaches close to unity at the final step. The second most stable structure, $J = 3$, is amplified once in the first 1500 steps and then turns to decrease. We draw the electronic wave function component contained in the most stable state, $J = 2$, in Fig. 9(c). The ground state $|\phi_{\rm gs}\rangle$ for the geometry $J = 2$ quickly increases, and the excited states decrease to zero within 1000 steps. These results support that our ideas of encoding candidate geometries for optimization work also for the variational scheme. The convergence of nuclear states was rather slow compared to that of the electronic states for the individual geometries, as seen in Figs. 9(b) and (c). This

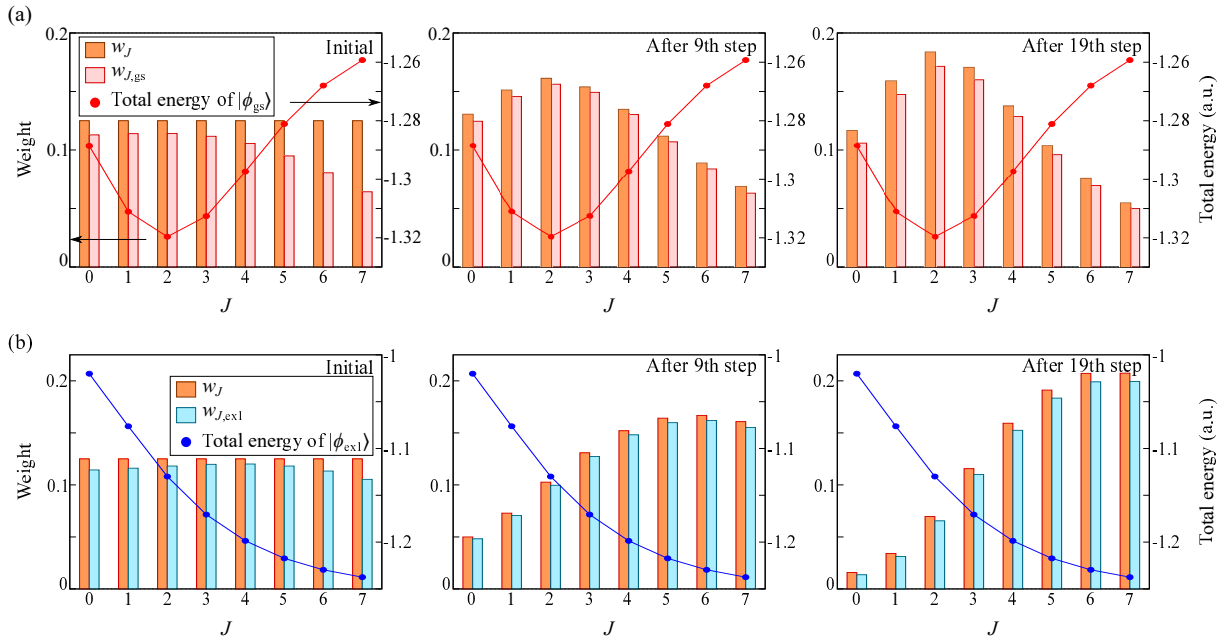

FIG. 7. (a) Simulation results of optimization for eight candidate geometries starting from the symmetric spatial wave function in Eq. (21). The boxes show the weight w_J of each geometry J during the PITE steps. The weight $w_{J,\mathrm{gs}}$ of the ground state for each geometry is also shown. The red circles represent the total energies of the ground states $|\psi_{\mathrm{gs}}\rangle$ for the geometries. (b) The results of simulation starting from the antisymmetric spatial wave function in Eq. (22), indicating the absence of equilibrium bond length for the first excited state $|\psi_{\mathrm{ex1}}\rangle$.

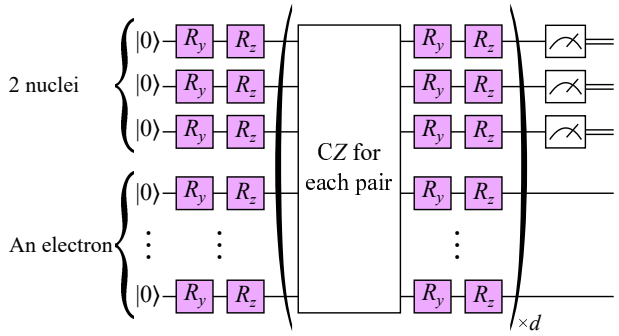

FIG. 8. Ansatz circuit for geometry optimization of the H_2^+ model system based on the VITE approach. The part inside the parentheses are applied to the nuclear and electronic registers d times. The purple boxes stand for single-qubit rotations whose angles are specified by distinct variational parameters. The nuclear register is measured at the end of the circuit to find the optimal bond length.

observation reflects the generic fact that the continuous energy of classical nuclei leads to a small energy difference between neighboring candidate geometries, as discussed in Sect. II B 2.

C. PITE for a classical C_6H_6-Ar system

1. Setup

As stated in Sect. II B 4, our scheme is also applicable to a geometry optimization problem for point charges as a classical system. It is known that the improved Lennard–Jones (ILJ)[41, 42] potentials describe the experimental data well for hydrocarbon molecules interacting with rare-gas atoms. We adopt here these model potentials to consider a system consisting of a benzene molecule interacting weakly with an argon atom[41], as depicted in Fig. 10(a). We perform simulations of geometry optimization for this system by using our PITE scheme.

The C-C and C-H bond lengths are fixed at 1.39 Å and 1.09 Å[43], respectively, throughout the simulations. The explicit expressions for the ILJ potentials are provided in Appendix C. Figure 10(b) shows the interaction energy between the C_6H_6 molecule and the Ar atom on the xz plane as a function of the position of the Ar atom. The interaction energy takes a minimum value at $z = 3.57$ Å with $x = y = 0$ Å[41].

2. Geometry optimization

We performed simulations of geometry optimization among 64 candidates represented by $n_{qn} = 3$ qubits for

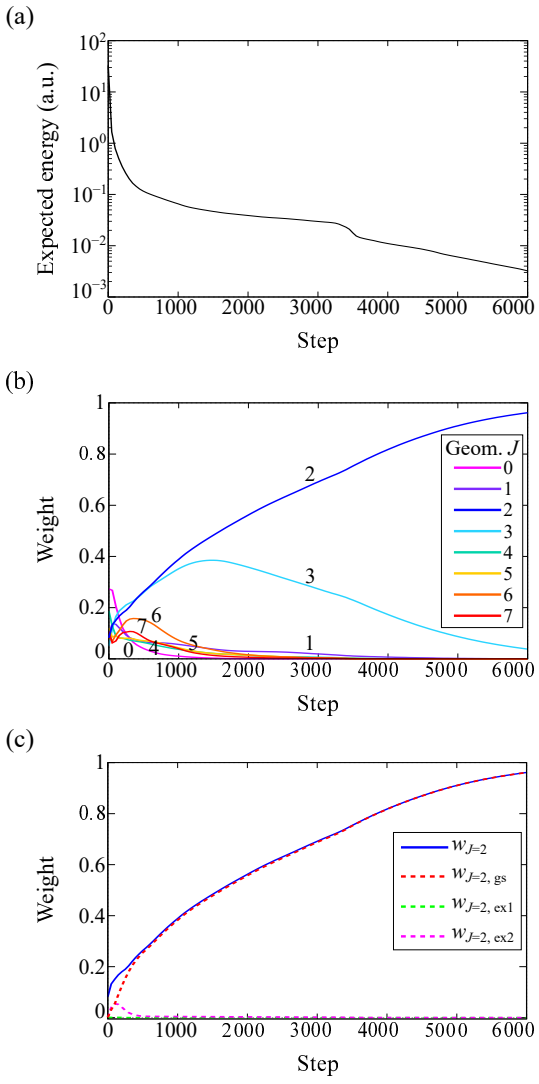

FIG. 9. (a) Expected energy of the trial state $|\Psi\rangle$ at each VITE step measured from the lowest energy eigenvalue of the molecule. (b) The weights w_J of candidate geometries contained in the trial state at each step. (c) The weight $w_{J=2,\mathrm{gs}}$ of the ground state $|\phi_{\mathrm{gs}}\rangle$ for the geometry $J = 2$ contained in the trial state at each step. Those of the first- and second-excited states, $w_{J=2,\mathrm{ex1}}$ and $w_{J=2,\mathrm{ex2}}$, are also shown.

each of the x and z coordinates of the Ar atom. Each of the candidates is specified by two integers $\boldsymbol{J} = (J_x, J_z)$ with $J_x, J_z = 0, \ldots, 7$, which generate the coordinates $x_{\boldsymbol{J}} = -2.4 + 0.8J_x$ Å and $z_{\boldsymbol{J}} = 3.2 + 0.4J_z$ Å. We used a constant amount $\Delta\tau = 0.004$ meV^{-1} of each PITE step in the following simulations.

In each simulation of the circuit shown in Fig. 3, we assigned a uniform weight distribution to the candidate geometries for an initial state. Figure 10(c) shows the weight $w_{\boldsymbol{J}}$ of each candidate during the steps contained in the state of nuclear register. It is seen that the uniform distribution of weights in the initial state undergoes the deformation via the steps, as expected. The largest weight is already seen after the 11th step at $\boldsymbol{J} = (3, 1)$, which is closer to the true optimal geometry than any other candidate is. This peak structure becomes more prominent after the 19th step, as seen in the figure.

IV. CONCLUSIONS

In summary, we have proposed a nonvariational scheme for geometry optimization of molecules within the framework of FQE, where the electrons and nuclei are treated as quantum mechanical particles and classical point charges, respectively. The outcomes of repeated measurements on the nuclear register accumulate to form the histogram possibly having multiple maxima, each of which corresponds to a local-minimum geometry. The scheme exhibits quantum advantage over any classical optimization scheme since the former employs the superposition of qubit states encoding both electronic states and molecular geometries. The circuit depth of RTE operation, which is the central component of each PITE step, was found to scale as $\mathcal{O}(n_e^2 \mathrm{poly}(\log n_e))$ for the electron number n_e. This can be reduced to $\mathcal{O}(n_e \mathrm{poly}(\log n_e))$ if the same number of extra qubits as in the original circuit are available. If $\mathcal{O}(n_e^2 \log n_e)$ extra qubits are available, the depth can be reduced to $\mathcal{O}(\mathrm{poly}(\log n_e))$. We confirmed the validity of the scheme via the numerical simulations for simple systems, including the classical system composed of charged particles. We also confirmed that the ideas of encoding candidate geometries work for the VITE approach, which will be helpful for realization of geometry optimization using NISQ devices.

In order for this scheme to be more efficient from a practical viewpoint, there may exist room for elaborating the sampling strategy for candidate geometries. That is, changing the range and resolution of nuclear displacements adaptively under a constraint of a fixed total number of measurements can enable us to determine the optimal geometry more accurately. Whether it is the case or not should be examined in the future.

ACKNOWLEDGMENTS

This work was supported by MEXT as "Program for Promoting Researches on the Supercomputer Fugaku" (JPMXP1020200205) and JSPS KAKENHI as "Grant-in-Aid for Scientific Research(A)" Grant Number 21H04553. The computation in this work has been done using (supercomputer Fugaku provided by the RIKEN Center for Computational Science/Supercomputer Center at the Institute for Solid State Physics in the University of Tokyo).

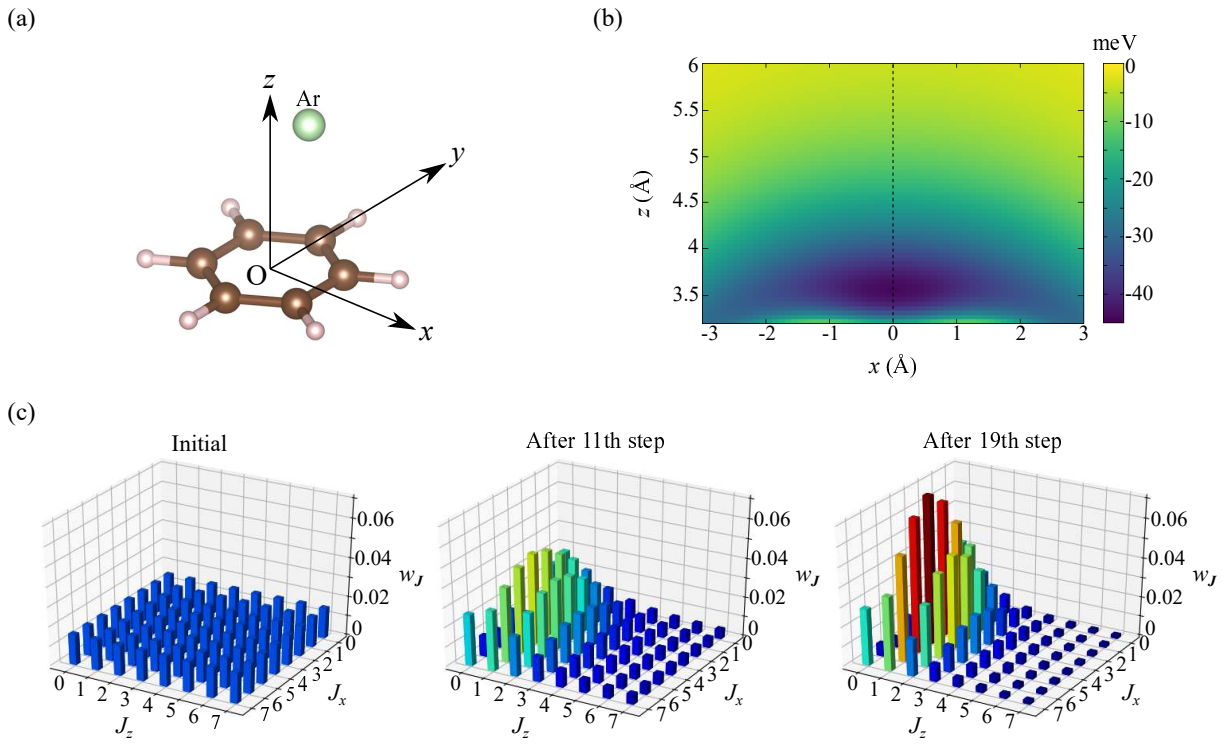

FIG. 10. (a) Classical target system for geometry optimization based on PITE approach. The C_6H_6 molecule lies on the xy plane with its center of mass located at the origin. Two of the C-H bonds are along the y axis. We consider an Ar atom on the xz plane. (b) The interaction energy as a function of the position of the Ar atom. (c) The weight of each candidate during the PITE steps contained in the state of nuclear register.

Appendix A: Implementation of phase gates in PITE circuit

1. Definition of phase gates

a. *Electron-electron phase gates*

To implement the evolution generated by $\hat{V}_{ee}$, we define the e-e phase gate U_{ee} such that it acts on a $6n_{qe}$-qubit state diagonally as

$$U_{ee}(\Delta t)\overbrace{|\boldsymbol{k}\rangle_{3n_{qe}}\otimes|\boldsymbol{k}'\rangle_{3n_{qe}}}^{\text{A pair of electrons}}\equiv\exp\left(-iv\left(\left|\boldsymbol{r}^{(\boldsymbol{k})}-\boldsymbol{r}^{(\boldsymbol{k}')}\right|\right)\Delta t\right)|\boldsymbol{k}\rangle_{3n_{qe}}\otimes|\boldsymbol{k}'\rangle_{3n_{qe}}. \tag{A1}$$

The evolution can thus be implemented by applying this phase gate to each of the possible pairs of n_e electrons:

$$e^{-i\hat{V}_{ee}\Delta t}=\prod_{\ell>\ell'}\overbrace{U_{ee}(\Delta t)}^{\text{On }\ell\text{th and }\ell'\text{th electrons}}, \tag{A2}$$

which requires the circuit depth on the order of $\mathcal{O}(n_e^2)$.

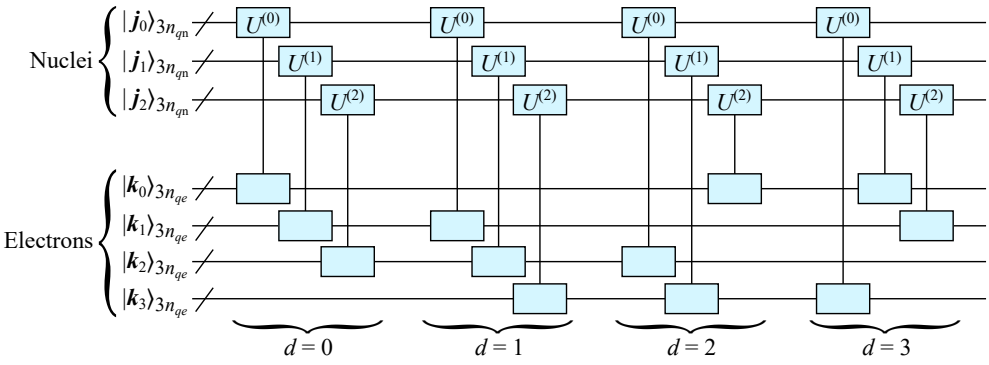

FIG. 11. Evolution operator $e^{-i\hat{V}_{\rm en}\Delta t}$ implemented based on Eq. (A4) for $n_e = 4$ and $n_{\rm nucl} = 3$. $U^{(\nu)}$ in this figure is a simplified notation of the phase gate $U^{(\nu)}_{\rm en}(\Delta t)$ tailored for the νth nucleus. It is depicted as connected two boxes.

b. *Electron-nucleus phase gates*

To implement the evolution generated by $\hat{V}_{\rm en}$, we define the e-n phase gate $U^{(\nu)}_{\rm en}$ for each nucleus ν such that it acts on a $(3n_{qe} + 3n_{qn})$-qubit state diagonally as

$$U^{(\nu)}_{\rm en}(\Delta t)\ \overbrace{|\boldsymbol{k}\rangle_{3n_{qe}}}^{\text{An electron}} \otimes \overbrace{|\boldsymbol{j}_\nu\rangle_{3n_{qn}}}^{\nu\text{th nucleus}} \equiv \exp\left(iZ_\nu v\left(\left|\boldsymbol{r}^{(\boldsymbol{k})} - \boldsymbol{R}_\nu(\boldsymbol{j}_\nu)\right|\right)\Delta t\right)|\boldsymbol{k}\rangle_{3n_{qe}} \otimes |\boldsymbol{j}_\nu\rangle_{3n_{qn}}. \tag{A3}$$

The evolution can thus be implemented by applying this phase gate to each of the possible pairs of n_e electrons and $n_{\rm nucl}$ nuclei:

$$\begin{aligned} e^{-i\hat{V}_{\rm en}\Delta t} &= \prod_{\ell=0}^{n_e-1}\prod_{\nu=0}^{n_{\rm nucl}-1} \overbrace{U^{(\nu)}_{\rm en}(\Delta t)}^{\text{On } \ell\text{th electron and } \nu\text{th nucleus}} \\ &= \prod_{d=0}^{n_e-1}\prod_{\nu=0}^{n_{\rm nucl}-1} \overbrace{U^{(\nu)}_{\rm en}(\Delta t)}^{\text{On } \ell\text{th electron and } \nu\text{th nucleus}}\Bigg|_{\ell=\nu+d \bmod n_e}, \end{aligned} \tag{A4}$$

where we used the generic relation $n_e \geq n_{\rm nucl}$ for a molecule to get the last equality. This expression allows us to implement the evolution with the circuit depth on the order of $\mathcal{O}(n_e^1 n_{\rm nucl}^0)$ since the gate operators for a common d can be performed simultaneously. Such an implementation for $n_e = 4$ and $n_{\rm nucl} = 3$ is shown in Fig. 11 as an example.

c. *Nucleus-nucleus phase gates*

To implement the evolution generated by $\hat{V}_{\rm nn}$, we define the n-n phase gate $U^{(\nu,\nu')}_{\rm nn}$ for each pair of nuclei ν and ν' such that it acts on a $6n_{qn}$-qubit state diagonally as

$$U^{(\nu,\nu')}_{\rm nn}(\Delta t)\ \overbrace{|\boldsymbol{j}_\nu\rangle_{3n_{qn}}}^{\nu\text{th nucleus}} \otimes \overbrace{|\boldsymbol{j}_{\nu'}\rangle_{3n_{qn}}}^{\nu'\text{th nucleus}} \equiv \exp\Big(-iZ_\nu Z_{\nu'} v\left(|\boldsymbol{R}_\nu(\boldsymbol{j}_\nu) - \boldsymbol{R}_{\nu'}(\boldsymbol{j}_{\nu'})|\right)\Delta t\Big)|\boldsymbol{j}_\nu\rangle_{3n_{qn}} \otimes |\boldsymbol{j}_{\nu'}\rangle_{3n_{qn}}. \tag{A5}$$

The evolution can thus be implemented by applying this phase gate to each of the possible pairs of $n_{\rm nucl}$ nuclei:

$$e^{-i\hat{V}_{\rm nn}\Delta t} = \prod_{\nu>\nu'} \overbrace{U^{(\nu,\nu')}_{\rm nn}(\Delta t)}^{\text{On } \nu\text{th and } \nu'\text{th nuclei}}, \tag{A6}$$

which requires the circuit depth on the order of $\mathcal{O}(n_{\rm nucl}^2)$.

d. External-field phase gates

To implement the evolution generated by $\hat{V}_{\rm ext}$, we define the phase gate $U_{\rm ext}$ such that it acts on a $3n_{qe}$-qubit state diagonally as

$$U_{\rm ext}(\Delta t) \overbrace{|\boldsymbol{k}\rangle_{3n_{qe}}}^{\text{An electron}} \equiv \exp\left(-iv_{\rm ext}(\boldsymbol{r}^{(\boldsymbol{k})})\Delta t\right)|\boldsymbol{k}\rangle_{3n_{qe}}. \tag{A7}$$

The evolution can thus be implemented by applying this phase gate to each of the n_e electrons:

$$e^{-i\hat{V}_{\rm ext}\Delta t} = \prod_{\ell=0}^{n_e-1} \overbrace{U_{\rm ext}(\Delta t)}^{\text{On } \ell\text{th electron}}, \tag{A8}$$

which requires the circuit depth on the order of $\mathcal{O}(1)$ since all the gate operations can be performed simultaneously.

2. Implementation using distance registers

a. Electron-electron distances

We introduce $n_{ee}^{(\rm d)}$ qubits, which we call the electron-electron distance register, and define the unitary $U_{ee}^{(\rm d)}$ such that it computes the distance between two electrons as

$$U_{ee}^{(\rm d)}\left(|\boldsymbol{k}\rangle_{3n_{qe}}\otimes|\boldsymbol{k}'\rangle_{3n_{qe}}\otimes|0\rangle_{n_{ee}^{(\rm d)}}\right) = |\boldsymbol{k}\rangle_{3n_{qe}}\otimes|\boldsymbol{k}'\rangle_{3n_{qe}}\otimes\left||\boldsymbol{r}^{(\boldsymbol{k})}-\boldsymbol{r}^{(\boldsymbol{k}')}|\right\rangle_{n_{ee}^{(\rm d)}}, \tag{A9}$$

where the rightmost ket on the RHS is the state of the distance register that stores the distance within some accuracy characterized by $n_{ee}^{(\rm d)}$.

b. Electron-nucleus distances

We define similarly the unitary $U_{\rm en}^{(\rm d,\nu)}$ for each ν that computes the distance between an electron and the νth nucleus and store it into $n_{\rm en}^{(\rm d)}$ qubits as

$$U_{\rm en}^{(\rm d,\nu)}\left(|\boldsymbol{k}\rangle_{3n_{qe}}\otimes|\boldsymbol{j}_\nu\rangle_{3n_{qn}}\otimes|0\rangle_{n_{\rm en}^{(\rm d)}}\right) = |\boldsymbol{k}\rangle_{3n_{qe}}\otimes|\boldsymbol{j}_\nu\rangle_{3n_{qn}}\otimes\left||\boldsymbol{r}^{(\boldsymbol{k})}-\boldsymbol{R}_\nu(\boldsymbol{j}_\nu)|\right\rangle_{n_{\rm en}^{(\rm d)}}, \tag{A10}$$

where $\boldsymbol{R}_\nu(\boldsymbol{j}_\nu)$ is the position of nucleus with the displacement $\boldsymbol{j}_\nu$.

c. Nucleus-nucleus distances

Also, we define the unitary $U_{\rm nn}^{(\rm d,\nu,\nu')}$ for each pair of ν and ν' that computes the distance between the pair of nuclei and store it into $n_{\rm nn}^{(\rm d)}$ qubits as

$$U_{\rm nn}^{(\rm d,\nu,\nu')}\left(|\boldsymbol{j}_\nu\rangle_{3n_{qn}}\otimes|\boldsymbol{j}_{\nu'}\rangle_{3n_{qn}}\otimes|0\rangle_{n_{\rm nn}^{(\rm d)}}\right) = |\boldsymbol{j}_\nu\rangle_{3n_{qn}}\otimes|\boldsymbol{j}_{\nu'}\rangle_{3n_{qn}}\otimes\left||\boldsymbol{R}_\nu(\boldsymbol{j}_\nu)-\boldsymbol{R}_{\nu'}(\boldsymbol{j}_{\nu'})|\right\rangle_{n_{\rm nn}^{(\rm d)}}. \tag{A11}$$

We assume that the electron-electron, electron-nucleus, and nucleus-nucleus distance registers encode approximate distances in a common manner despite the different numbers of constituent qubits.

d. Phase gates for interaction as a function of a distance

We define the interaction phase gate $U_{{\rm int},\kappa}(\Delta t)$ ($\kappa = ee, e{\rm n}, {\rm nn}$) for a distance register composed of $n_\kappa^{(\rm d)}$ qubits such that it acts diagonally as

$$U_{{\rm int},\kappa}(\Delta t)|r\rangle_{n_\kappa^{(\rm d)}} = e^{-iv(r)\Delta t}|r\rangle_{n_\kappa^{(\rm d)}}, \tag{A12}$$

where the ket encodes the argument of v.

e. Circuits for pairwise phase gates

Having introduced the unitaries for the distances between particles and the interaction v, we are now able to construct the circuits for the pairwise phase gates appearing in Eqs. (A2), (A4), and (A6). Specifically, the e-e phase gate for an electron pair defined in Eq. (A1) can be expressed as

$$U_{ee}(\Delta t) = U_{ee}^{(\mathrm{d})\dagger} U_{\mathrm{int},ee}(\Delta t) U_{ee}^{(\mathrm{d})}, \tag{A13}$$

leading to the circuit shown in Fig. 5. This circuit acts on the $6n_{qe} + n_{ee}^{(\mathrm{d})}$ qubits via the following three steps: computation of the distance, generation of the phase, and uncomputation for disentangling the distance register from the electronic register, that is,

$$\begin{aligned} |\boldsymbol{k}\rangle_{3n_{qe}} \otimes |\boldsymbol{k}'\rangle_{3n_{qe}} \otimes |0\rangle_{n_{ee}^{(\mathrm{d})}} &\xmapsto{\text{Distance}} |\boldsymbol{k}\rangle_{3n_{qe}} \otimes |\boldsymbol{k}'\rangle_{3n_{qe}} \otimes \left| |\boldsymbol{r}^{(\boldsymbol{k})} - \boldsymbol{r}^{(\boldsymbol{k}')}| \right\rangle_{n_{ee}^{(\mathrm{d})}} \\ &\xmapsto{\text{Phase}} |\boldsymbol{k}\rangle_{3n_{qe}} \otimes |\boldsymbol{k}'\rangle_{3n_{qe}} \otimes e^{iv(r)\Delta t} |r\rangle_{n_{ee}^{(\mathrm{d})}} \Big|_{r=|\boldsymbol{r}^{(\boldsymbol{k})} - \boldsymbol{r}^{(\boldsymbol{k}')}|} \\ &\xmapsto{\text{Distance}^\dagger} e^{iv(|\boldsymbol{r}^{(\boldsymbol{k})} - \boldsymbol{r}^{(\boldsymbol{k}')}|)\Delta t} |\boldsymbol{k}\rangle_{3n_{qe}} \otimes |\boldsymbol{k}'\rangle_{3n_{qe}} \otimes |0\rangle_{n_{ee}^{(\mathrm{d})}}. \end{aligned} \tag{A14}$$

Since the distance register has been initialized again, it can be recycled for other pairs of electrons.

The e-n phase gate for an electron-nucleus pair defined in Eq. (A3) can be expressed as

$$U_{\mathrm{en}}^{(\nu)}(\Delta t) = U_{\mathrm{en}}^{(\mathrm{d},\nu)\dagger} U_{\mathrm{int,en}}(-Z_\nu \Delta t) U_{\mathrm{en}}^{(\mathrm{d},\nu)}, \tag{A15}$$

while the n-n phase gate for a nucleus pair defined in Eq. (A5) can be expressed as

$$U_{\mathrm{nn}}^{(\nu,\nu')}(\Delta t) = U_{\mathrm{nn}}^{(\mathrm{d},\nu,\nu')\dagger} U_{\mathrm{int,nn}}(Z_\nu Z_{\nu'} \Delta t) U_{\mathrm{nn}}^{(\mathrm{d},\nu,\nu')}. \tag{A16}$$

The circuits for these pairwise phase gates can also be constructed similarly to the case of an electron pair.

3. Efficient implementation of electron-electron evolution using a redundant register

If the same number of qubits as in the electronic register are available, we can reduce the scaling of circuit depth for the evolution $e^{-i\hat{V}_{ee}\Delta t}$ generated by the electron-electron interactions. Although the technique explained below is essentially the same as that in Ref. [23], we describe it in order for this paper to be self contained.

For the electronic register consisting of $3n_e n_{qe}$ qubits, we construct the circuit shown in Fig. 12(a) by introducing an extra register consisting of $3n_e n_{qe}$ qubits denoted as a redundant register. The $6n_e n_{qe}$-qubit system composed of the electronic register encoding a generic state in Eq. (2) and the initialized redundant register undergoes the operations

as

$$
\begin{aligned}
&\overbrace{|\psi\rangle}^{\text{Electrons}} \otimes \overbrace{|0\rangle_{3n_en_{qe}}}^{\text{Redundant}} \\
&\xmapsto{\text{CNOTs}} \Delta V^{n_e/2} \sum_{\boldsymbol{K}} \psi(\boldsymbol{r}^{(\boldsymbol{k}_0)}, \ldots, \boldsymbol{r}^{(\boldsymbol{k}_{n_e-1})}) |\boldsymbol{K}\rangle_{3n_en_{qe}} \otimes |\boldsymbol{K}\rangle_{3n_en_{qe}} \\
&\xmapsto{\text{Phase}} \prod_{\substack{\ell>\ell' \\ \ell\in\text{Electron reg.} \\ \ell'\in\text{Redundant reg.}}} \overbrace{U_{ee}(\Delta t)}^{\text{On } \ell\text{th and } \ell'\text{th electrons}} \Delta V^{n_e/2} \sum_{\boldsymbol{K}} \psi(\boldsymbol{r}^{(\boldsymbol{k}_0)}, \ldots, \boldsymbol{r}^{(\boldsymbol{k}_{n_e-1})}) |\boldsymbol{K}\rangle_{3n_en_{qe}} \otimes |\boldsymbol{K}\rangle_{3n_en_{qe}} \\
&= \prod_{\substack{\ell>\ell' \\ \ell\in\text{Electron reg.} \\ \ell'\in\text{Redundant reg.}}} \Delta V^{n_e/2} \sum_{\boldsymbol{K}} \psi(\boldsymbol{r}^{(\boldsymbol{k}_0)}, \ldots, \boldsymbol{r}^{(\boldsymbol{k}_{n_e-1})}) \exp\left(-iv\left(\left|\boldsymbol{r}^{(\boldsymbol{k}_\ell)} - \boldsymbol{r}^{(\boldsymbol{k}_{\ell'})}\right|\right)\Delta t\right) |\boldsymbol{K}\rangle_{3n_en_{qe}} \otimes |\boldsymbol{K}\rangle_{3n_en_{qe}} \\
&= \prod_{\substack{\ell>\ell' \\ \ell,\ell'\in\text{Electron reg.}}} \Delta V^{n_e/2} \sum_{\boldsymbol{K}} \psi(\boldsymbol{r}^{(\boldsymbol{k}_0)}, \ldots, \boldsymbol{r}^{(\boldsymbol{k}_{n_e-1})}) \exp\left(-iv\left(\left|\boldsymbol{r}^{(\boldsymbol{k}_\ell)} - \boldsymbol{r}^{(\boldsymbol{k}_{\ell'})}\right|\right)\Delta t\right) |\boldsymbol{K}\rangle_{3n_en_{qe}} \otimes |\boldsymbol{K}\rangle_{3n_en_{qe}} \\
&\xmapsto{\text{CNOTs}} \prod_{\substack{\ell>\ell' \\ \ell,\ell'\in\text{Electron reg.}}} \Delta V^{n_e/2} \sum_{\boldsymbol{K}} \psi(\boldsymbol{r}^{(\boldsymbol{k}_0)}, \ldots, \boldsymbol{r}^{(\boldsymbol{k}_{n_e-1})}) \exp\left(-iv\left(\left|\boldsymbol{r}^{(\boldsymbol{k}_\ell)} - \boldsymbol{r}^{(\boldsymbol{k}_{\ell'})}\right|\right)\Delta t\right) |\boldsymbol{K}\rangle_{3n_en_{qe}} \otimes |0\rangle_{3n_en_{qe}} \\
&= \left(e^{-i\hat{V}_{ee}\Delta t}|\psi\rangle\right) \otimes |0\rangle_{3n_en_{qe}},
\end{aligned}
\tag{A17}
$$

where the redundant register in the final state can be discarded safely since it is disentangled from the electronic register. The central part of this circuit is composed of the $n_e(n_e-1)/2$ electron-electron phase gates $U_{ee}(\Delta t)$. Their sequence can be written as

$$
\prod_{\substack{\ell>\ell' \\ \ell\in\text{Electron reg.} \\ \ell'\in\text{Redundant reg.}}} \overbrace{U_{ee}(\Delta t)}^{\text{On } \ell\text{th and } \ell'\text{th electrons}} = \prod_{\ell'\in\text{Redundant reg.}} \prod_{d=1}^{n_e-1-\ell'} \overbrace{U_{ee}(\Delta t)}^{\text{On } (\ell'+d)\text{th and } \ell'\text{th electrons}}, \tag{A18}
$$

which means that the $n_e - 1$ phase gates for a fixed d can be performed simultaneously. This fact enables us to implement the evolution with the depth $\mathcal{O}(n_e)$ in terms of the electron number. Fig. 12(b) shows the circuit for the case of $n_e = 4$ as an example. This technique is applicable not only to electronic simulations but also to other kinds of quantum algorithms that impose all-to-all connectivity on qubits.

Appendix B: Review of VITE approach

For solving the imaginary-time Schrödinger equation in the VQE manner, we approximate the solution as $|\Psi(\tau)\rangle \approx |\Phi(\boldsymbol{\theta}(\tau))\rangle$ expressed with n_p real parameters $\boldsymbol{\theta}(\tau)$ specified by a single real parameter τ, referred to as an imaginary time. In the language of quantum computation, $\boldsymbol{\theta}$ are the circuit parameters characterizing an adopted ansatz. Here, we use the McLachlan's variational principle[44] to derive the equation of motion for $\boldsymbol{\theta}$. By using the expected energy $E_\tau \equiv \langle\Phi(\boldsymbol{\theta}(\tau))|\mathcal{H}|\Phi(\boldsymbol{\theta}(\tau))\rangle$ for a fixed state $|\Phi(\boldsymbol{\theta}(\tau))\rangle$ at a given τ for the Hamiltonian $\mathcal{H}$, the requirement that the distance between derivative $\partial|\Phi(\boldsymbol{\theta}(\tau))\rangle/\partial\tau$ and $-(\mathcal{H} - E_\tau)|\Phi(\boldsymbol{\theta}(\tau))\rangle$ should be a stationary value is expressed as[17]

$$
\delta \left\| \left(\frac{\partial}{\partial\tau} + \mathcal{H} - E_\tau\right) |\Phi(\boldsymbol{\theta}(\tau))\rangle \right\|^2 = 0. \tag{B1}
$$

This equation is solved under the constraint $\||\Phi(\boldsymbol{\theta}(\tau))\rangle\|^2 = 1$ for normalization. Accordingly, by executing the variation, we obtain the equation governing the evolution of the parameters:

$$
\mathcal{M}(\tau)\frac{d\boldsymbol{\theta}(\tau)}{d\tau} = \boldsymbol{\mathcal{V}}(\tau) \tag{B2}
$$

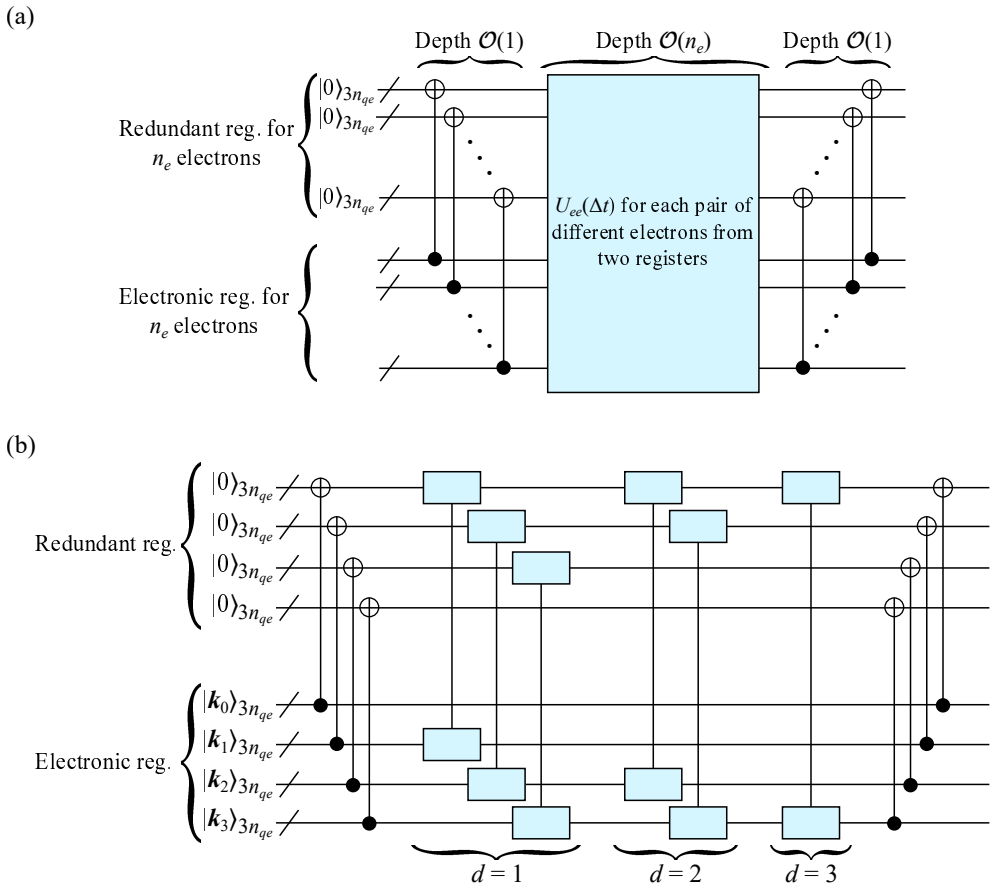

FIG. 12. (a) Efficient implementation of $e^{-i\hat{V}_{ee}\Delta t}$ for n_e electrons by using a redundant register consisting of the same number of qubits as in the electronic register. Each of the CNOT symbols on the circuit means that the $3n_{qe}$ qubits for each electron in the electronic register are coupled via CNOT operations to the corresponding qubits in the redundant register. The scaling of depths with respect to n_e is also shown. (b) The implementation of evolution for $n_e = 4$. Each pair of connected boxes on the circuit represents the electron-electron phase gate $U_{ee}(\Delta t)$, defined in Eq. (A1).

where the matrix

$$\mathcal{M}_{jj'}(\tau) = \mathrm{Re}\left\langle \frac{\partial\Phi(\boldsymbol{\theta})}{\partial\theta_j}\middle|\frac{\partial\Phi(\boldsymbol{\theta})}{\partial\theta_{j'}}\right\rangle\Bigg|_{\boldsymbol{\theta}=\boldsymbol{\theta}(\tau)} \tag{B3}$$

and the vector

$$\mathcal{V}_j(\tau) = -\,\mathrm{Re}\left\langle \frac{\partial\Phi(\boldsymbol{\theta})}{\partial\theta_j}\middle|\mathcal{H}\middle|\Phi(\boldsymbol{\theta})\right\rangle\Bigg|_{\boldsymbol{\theta}=\boldsymbol{\theta}(\tau)} \tag{B4}$$

for $j, j' = 0, \ldots, n_\mathrm{p} - 1$ were introduced. From Eq (B2), the parameters are updated from a finite difference $\Delta\tau$ of the imaginary time as $\boldsymbol{\theta}(\tau + \Delta\tau) = \boldsymbol{\theta}(\tau) + \Delta\tau\mathcal{M}^{-1}(\tau)\boldsymbol{\mathcal{V}}(\tau)$ within the first-order accuracy of $\Delta\tau$.

Next, we have to evaluate $\mathcal{M}(\tau)$ and $\mathcal{V}(\tau)$ for Eq. (B2) by using the quantum computer. We consider here a case where the variational parameters for a trial n_q-qubit wave function enter only via single-qubit rotation gates $R_\mu(\theta) = e^{-i\theta\sigma_\mu/2}$ with $\mu = x, y, z$. The analytic gradients of a parametrized unitary are presented in Ref[45]. Specifically, the derivative of an n-parameter unitary of the form $\mathcal{U}(\boldsymbol{\theta}) = \mathcal{U}(\theta_1, \ldots, \theta_{k-1})R_\mu(\theta_k)\mathcal{U}'(\theta_{k+1}, \ldots, \theta_{n_\mathrm{p}})$ with respect to the kth parameter is given obviously as

$$\frac{\partial\mathcal{U}(\boldsymbol{\theta})}{\partial\theta_k} = -\frac{i}{2}\mathcal{U}(\theta_1, \ldots, \theta_{k-1})\sigma_\mu R_\mu(\theta_k)\mathcal{U}'(\theta_{k+1}, \ldots, \theta_{n_\mathrm{p}}). \tag{B5}$$

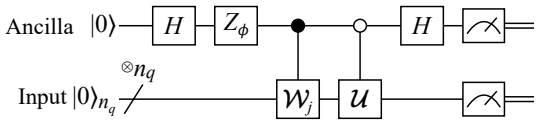

FIG. 13. Circuit for calculation of $\mathrm{Im}\langle 0|_{n_q}\mathcal{W}_j^\dagger\hat{V}\mathcal{U}|0\rangle_{n_q}$. H is the Hadamard gate. $Z_\phi = \mathrm{diag}(1, e^{i\phi})$ is a phase gate.

The inner product of different circuits for obtaining $\mathcal{M}_{jj'}(\tau)$ can be evaluated using, for example, the Hadamard test[46].

The remaining quantities we have to compute are E_τ and $\boldsymbol{\mathcal{V}}(\tau)$. We briefly explain the methodology presented by Ollitrault et al. [47], but of course, the method presented in Ref. [20] can be adopted. The Hamiltonian $\mathcal{H}$ in our case is decomposed into the kinetic and potential parts as in Eq. (1). Since the potential term is diagonal for the computational basis, the expectation value for the potential part can be computed from repeated measurements on the trial state using computational bases. On the contrary, the kinetic part is diagonal for the momentum basis. Thus, we can evaluate the expectation value for the kinetic part by applying the QFT to the trial state immediately before performing a measurement. In the following, we discuss the details for evaluating the matrix element for a potential operator $\hat{V}$. First, we write the derivative of the parameterized circuit as $|\partial_j\mathcal{U}(\boldsymbol{\theta})\rangle \equiv -(i/2)\mathcal{W}_j(\boldsymbol{\theta})|0\rangle_{n_q}$. What we have to evaluate is then, from Eq. (B4), $\mathrm{Im}\langle 0|_{n_q}\mathcal{W}_j(\boldsymbol{\theta}(\tau))^\dagger\hat{V}\mathcal{U}(\boldsymbol{\theta}(\tau))|0\rangle_{n_q}$. It can be obtained from the circuit shown in Fig. 13 that uses one ancillary qubit. For simplicity, we denote $\mathcal{U}(\boldsymbol{\theta}(\tau))$ and $\mathcal{W}_j(\boldsymbol{\theta}(\tau))$ by $\mathcal{U}$ and $\mathcal{W}_j$, respectively. The Z_ϕ is the phase gate. The input state $|0\rangle \otimes |0\rangle_{n_q}$ changes throughout the circuit as

$$\frac{1}{2}\sum_{s=0,1}|s\rangle \otimes \left(\mathcal{W}_j + (-1)^s e^{i\phi}\mathcal{U}\right)|0\rangle_{n_q}. \tag{B6}$$

The probability for finding $|s\rangle \otimes |k\rangle_{n_q}$ $(k = 0, \ldots, 2^{n_q} - 1)$ when we measure all the qubits is thus calculated as

$$\mathbb{P}_{s,k}^{(j)} = \frac{1}{4}\left|\langle k|_{n_q}\mathcal{W}_j|0\rangle_{n_q}\right|^2 + \frac{1}{4}\left|\langle k|_{n_q}\mathcal{U}|0\rangle_{n_q}\right|^2 + \frac{(-1)^s}{2}\left(\cos\phi\,\mathrm{Re}\,v_k^{(j)} - \sin\phi\,\mathrm{Im}\,v_k^{(j)}\right), \tag{B7}$$

where $v_k^{(j)} \equiv \langle 0|_{n_q}\mathcal{W}_j^\dagger|k\rangle_{n_q}\langle k|_{n_q}\mathcal{U}|0\rangle_{n_q}$ Finally, by setting $\phi = \pi/2$, we get the target value from the probabilities $\mathbb{P}_{s,k}^{(j)}$ for all the combinations of s and k as follows:

$$\sum_{s,k}(-1)^s\langle k|_{n_q}\hat{V}|k\rangle_{n_q}\mathbb{P}_{s,k}^{(j)} = -\,\mathrm{Im}\langle 0|_{n_q}\mathcal{W}_j^\dagger\hat{V}\mathcal{U}|0\rangle_{n_q}. \tag{B8}$$

Appendix C: ILJ potentials for a C_6H_6-Ar system

The interaction energy between a hydrocarbon molecule and a rare-gas atom a based on the ILJ potentials[41] is calculated from the additive pairwise contributions: $E_{\mathrm{int}} = \sum_b V_{ab}^{(\mathrm{ILJ})}$, where b runs over the bonds forming the molecule. The expression for each atom-bond pair is given by

$$V_{ab}^{(\mathrm{ILJ})} = \frac{D}{n(s) - m}\left(\frac{m}{s^{n(s)}} - \frac{n(s)}{s^m}\right). \tag{C1}$$

$D \equiv D_{ab\perp}\sin^2\theta_{ab} + D_{ab\parallel}\cos^2\theta_{ab}$ and $\lambda_{ab} \equiv \lambda_{ab\perp}\sin^2\theta_{ab} + \lambda_{ab\parallel}\cos^2\theta_{ab}$ have been introduced for taking into account the anisotropicity of relative position of a and b with the Jacobi angle θ_{ab} between the bond vector and the vector connecting the bond center $\boldsymbol{R}_b$ and the atom a at $\boldsymbol{R}_a$. $s \equiv |\boldsymbol{R}_a - \boldsymbol{R}_b|/\lambda_{ab}$ is the dimensionless argument for the radial potential. $D_{ab\parallel}$ and $\lambda_{ab\parallel}$ ($D_{ab\perp}$ and $\lambda_{ab\perp}$) are the depth of potential well and its location, respectively, when $\theta = 0$ ($\theta = \pi/2$). We adopted $\beta = 10$ for $n(s) \equiv \beta + 4s^2$ and $m = 6$ for the C_6H_6-Ar system as in the original paper. The parameters for bond-atom pairs for this system are as follows[41]: $\lambda_{\mathrm{Ar,CC}\perp} = 3.879$ Å, $\lambda_{\mathrm{Ar,CC}\parallel} = 4.189$ Å, $D_{\mathrm{Ar,CC}\perp} = 3.895$ meV, $D_{\mathrm{Ar,CC}\parallel} = 4.910$ meV, $\lambda_{\mathrm{Ar,CH}\perp} = 3.641$ Å, $\lambda_{\mathrm{Ar,CH}\parallel} = 3.851$ Å, $D_{\mathrm{Ar,CH}\perp} = 4.814$ meV, and $D_{\mathrm{Ar,CH}\parallel} = 3.981$ meV.

[1] S. Axelrod, D. Schwalbe-Koda, S. Mohapatra, J. Damewood, K. P. Greenman, and R. Gómez-Bombarelli, Learning matter: Materials design

with machine learning and atomistic simulations, Accounts of Materials Research **3**, 343 (2022).
[2] J. M. Pereira, M. Vieira, and S. M. Santos, Step-by-step design of proteins for small molecule interaction: A review on recent milestones, Protein Science **30**, 1502 (2021), https://onlinelibrary.wiley.com/doi/pdf/10.1002/pro.4098.
[3] M. Pandey, M. Fernandez, F. Gentile, O. Isayev, A. Tropsha, A. C. Stern, and A. Cherkasov, The transformational role of gpu computing and deep learning in drug discovery, Nature Machine Intelligence **4**, 211 (2022).
[4] P. Hohenberg and W. Kohn, Inhomogeneous electron gas, Phys. Rev. **136**, B864 (1964).
[5] W. Kohn and L. J. Sham, Self-consistent equations including exchange and correlation effects, Phys. Rev. **140**, A1133 (1965).
[6] T. Helgaker, P. Jørgensen, and J. Olsen, *Molecular Electronic-Structure Theory* (Wiley, 2000).
[7] R. P. Feynman, Forces in molecules, Phys. Rev. **56**, 340 (1939).
[8] P. Pulay, Ab initio calculation of force constants and equilibrium geometries in polyatomic molecules, Molecular Physics **17**, 197 (1969), https://doi.org/10.1080/00268976900100941.
[9] H. B. Schlegel, Geometry optimization, WIREs Computational Molecular Science **1**, 790 (2011), https://wires.onlinelibrary.wiley.com/doi/pdf/10.1002/wcms.34.
[10] R. P. Feynman, Simulating physics with computers, International Journal of Theoretical Physics **21**, 467 (1982).
[11] H. Hirai, T. Horiba, S. Shirai, K. Kanno, K. Omiya, Y. O. Nakagawa, and S. Koh, Molecular structure optimization based on electrons–nuclei quantum dynamics computation, ACS Omega **7**, 19784 (2022), https://doi.org/10.1021/acsomega.2c01546.
[12] S. Wiesner, Simulations of Many-Body Quantum Systems by a Quantum Computer, arXiv e-prints , quant-ph/9603028 (1996), arXiv:quant-ph/9603028 [quant-ph].
[13] C. Zalka, Simulating quantum systems on a quantum computer, Proceedings of the Royal Society of London. Series A: Mathematical, Physical and Engineering Sciences **454**, 313 (1998), https://royalsocietypublishing.org/doi/pdf/10.1098/rspa.1998.0162.
[14] I. Kassal, S. P. Jordan, P. J. Love, M. Mohseni, and A. Aspuru-Guzik, Polynomial-time quantum algorithm for the simulation of chemical dynamics, Proceedings of the National Academy of Sciences **105**, 18681 (2008), https://www.pnas.org/content/105/48/18681.full.pdf.
[15] T. Jones, S. Endo, S. McArdle, X. Yuan, and S. C. Benjamin, Variational quantum algorithms for discovering hamiltonian spectra, Phys. Rev. A **99**, 062304 (2019).
[16] S. McArdle, T. Jones, S. Endo, Y. Li, S. C. Benjamin, and X. Yuan, Variational ansatz-based quantum simulation of imaginary time evolution, npj Quantum Information **5**, 75 (2019).
[17] X. Yuan, S. Endo, Q. Zhao, Y. Li, and S. C. Benjamin, Theory of variational quantum simulation, Quantum **3**, 191 (2019).
[18] A. Peruzzo, J. McClean, P. Shadbolt, M.-H. Yung, X.-Q. Zhou, P. J. Love, A. Aspuru-Guzik, and J. L. O'Brien, A variational eigenvalue solver on a photonic quantum processor, Nature Communications **5**, 4213 EP (2014), article.
[19] J. R. McClean, J. Romero, R. Babbush, and A. Aspuru-Guzik, The theory of variational hybrid quantum-classical algorithms, New Journal of Physics **18**, 023023 (2016).
[20] T. Kosugi, Y. Nishiya, H. Nishi, and Y.-i. Matsushita, Imaginary-time evolution using forward and backward real-time evolution with a single ancilla: First-quantized eigensolver algorithm for quantum chemistry, Phys. Rev. Research **4**, 033121 (2022).
[21] T. Kosugi and Y.-i. Matsushita, Construction of green's functions on a quantum computer: Quasiparticle spectra of molecules, Phys. Rev. A **101**, 012330 (2020).
[22] T. Kosugi and Y.-i. Matsushita, Linear-response functions of molecules on a quantum computer: Charge and spin responses and optical absorption, Phys. Rev. Research **2**, 033043 (2020).
[23] N. C. Jones, J. D. Whitfield, P. L. McMahon, M.-H. Yung, R. V. Meter, A. Aspuru-Guzik, and Y. Yamamoto, Faster quantum chemistry simulation on fault-tolerant quantum computers, New Journal of Physics **14**, 115023 (2012).
[24] H. H. S. Chan, R. Meister, T. Jones, D. P. Tew, and S. C. Benjamin, Grid-based methods for chemistry modelling on a quantum computer, arXiv e-prints , arXiv:2202.05864 (2022), arXiv:2202.05864 [quant-ph].
[25] D. S. Abrams and S. Lloyd, Simulation of many-body fermi systems on a universal quantum computer, Phys. Rev. Lett. **79**, 2586 (1997).
[26] D. W. Berry, M. Kieferová, A. Scherer, Y. R. Sanders, G. H. Low, N. Wiebe, C. Gidney, and R. Babbush, Improved techniques for preparing eigenstates of fermionic hamiltonians, npj Quantum Information **4**, 22 (2018).
[27] R. D. Somma, Quantum simulations of one dimensional quantum systems, arXiv e-prints , arXiv:1503.06319 (2015), arXiv:1503.06319 [quant-ph].
[28] P. J. Ollitrault, G. Mazzola, and I. Tavernelli, Nonadiabatic molecular quantum dynamics with quantum computers, Phys. Rev. Lett. **125**, 260511 (2020).
[29] T. G. Draper, Addition on a Quantum Computer, arXiv e-prints , quant-ph/0008033 (2000), arXiv:quant-ph/0008033 [quant-ph].
[30] T. G. Draper, S. A. Kutin, E. M. Rains, and K. M. Svore, A logarithmic-depth quantum carry-lookahead adder, arXiv e-prints , quant-ph/0406142 (2004), arXiv:quant-ph/0406142 [quant-ph].
[31] A. Parent, M. Roetteler, and M. Mosca, Improved reversible and quantum circuits for Karatsuba-based integer multiplication, arXiv e-prints , arXiv:1706.03419 (2017), arXiv:1706.03419 [quant-ph].
[32] L. A. B. Kowada, R. Portugal, and C. M. H. de Figueiredo, Reversible karatsuba's algorithm, Journal of Universal Computer Science **12**, 499 (2006).
[33] A. Parent, M. Roetteler, and M. Mosca, Improved reversible and quantum circuits for Karatsuba-based integer multiplication, arXiv e-prints , arXiv:1706.03419 (2017), arXiv:1706.03419 [quant-ph].
[34] S. Dutta, D. Bhattacharjee, and A. Chattopadhyay, Quantum circuits for toom-cook multiplication, Phys. Rev. A **98**, 012311 (2018).
[35] S. Hadfield, Quantum Algorithms for Scientific Computing and Approximate Optimization, arXiv e-prints , arXiv:1805.03265 (2018), arXiv:1805.03265 [quant-ph].
[36] G. Benenti and G. Strini, Quantum simulation of the single-particle schrödinger equation, American Journal of Physics **76**, 657 (2008), https://doi.org/10.1119/1.2894532.
[37] D. G. Tempel, T. J. Martínez, and N. T.

Maitra, Revisiting molecular dissociation in density functional theory: A simple model, Journal of Chemical Theory and Computation **5**, 770 (2009).

[38] C. Li, Exact analytical solution of the ground-state hydrogenic problem with soft coulomb potential, The Journal of Physical Chemistry A **125**, 5146 (2021), pMID: 34096283, https://doi.org/10.1021/acs.jpca.1c00698.

[39] L. O. Wagner, E. M. Stoudenmire, K. Burke, and S. R. White, Reference electronic structure calculations in one dimension, Phys. Chem. Chem. Phys. **14**, 8581 (2012).

[40] A. Kandala, A. Mezzacapo, K. Temme, M. Takita, M. Brink, J. M. Chow, and J. M. Gambetta, Hardware-efficient variational quantum eigensolver for small molecules and quantum magnets, Nature **549**, 242 (2017).

[41] F. Pirani, M. Alberti, A. Castro, M. Teixidor, and D. Cappelletti, Atom–bond pairwise additive representation for intermolecular potential energy surfaces, Chemical Physics Letters **394**, 37 (2004).

[42] F. Pirani, S. Brizi, L. F. Roncaratti, P. Casavecchia, D. Cappellettigege, and F. Vecchiocattivi, Beyond the lennard-jones model: a simple and accurate potential function probed by high resolution scattering data useful for molecular dynamics simulations, Physical Chemistry Chemical Physics **10**, 5489 (2008).

[43] F. Pirani, M. Porrini, S. Cavalli, M. Bartolomei, and D. Cappellettigaga, Potential energy surfaces for the benzene–rare gas systems, Chemical Physics Letters **367**, 405 (2003).

[44] A. McLachlan, A variational solution of the time-dependent schrodinger equation, Molecular Physics **8**, 39 (1964).

[45] M. Schuld, V. Bergholm, C. Gogolin, J. Izaac, and N. Killoran, Evaluating analytic gradients on quantum hardware, Phys. Rev. A **99**, 032331 (2019).

[46] K. Mitarai and K. Fujii, Methodology for replacing indirect measurements with direct measurements, Phys. Rev. Research **1**, 013006 (2019).

[47] P. J. Ollitrault, S. Jandura, A. Miessen, I. Burghardt, R. Martinazzo, F. Tacchino, and I. Tavernelli, Quantum algorithms for grid-based variational time evolution, arXiv preprint arXiv:2203.02521 10.48550/ARXIV.2203.02521 (2022).